

# 1 Seismo-acoustic and GNSS monitoring of a record-breaking storm 2 in the Black Sea: Evidence of climate change and intensifying 3 natural hazards

4  
5 Laura Petrescu<sup>1,2,\*</sup>, Bogdan Antonescu<sup>1,2</sup>, Sorin Nistor<sup>3</sup>, Iustin Floroiu<sup>4,5</sup>, Dragoş Ene<sup>1</sup>, Daniela  
6 Ghica<sup>1</sup>, Constantin Ionescu<sup>1</sup>, Andrei Anghel<sup>4</sup>, Mihai Datcu<sup>4</sup>

- 7  
8 1. National Institute for Earth Physics, Magurele, Romania  
9 2. University of Bucharest, Faculty of Physics, Magurele, Romania  
10 3. University of Oradea, Faculty of Construction, Cadaster and Architecture, Oradea,  
11 Romania  
12 4. Politehnica University of Bucharest, Faculty of Electronics, Telecommunications and  
13 Information Technology, Bucharest, Romania  
14 5. Politehnica University of Bucharest, Doctoral School of Electronics,  
15 Telecommunications & Information Technology, Bucharest, Romania

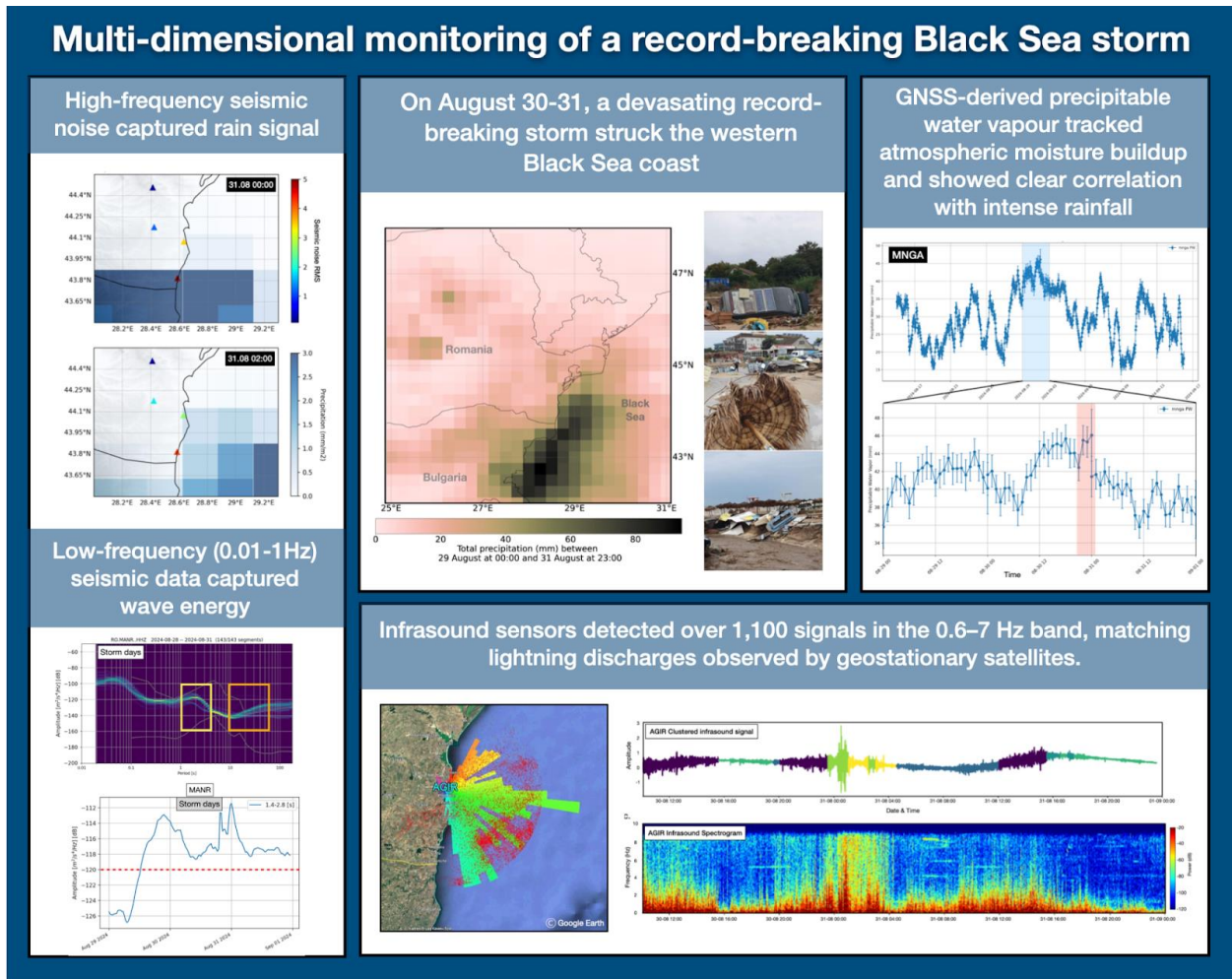
16 \* laura.petrescu@infp.ro

## 17 18 Abstract

19  
20 In August 2024, a devastating storm struck Romania's Black Sea coast, setting new precipitation  
21 records and highlighting the increasing frequency of extreme weather events. This study explores  
22 the integration of non-conventional sensors (seismic, GNSS, infrasound, and satellite data) with  
23 ERA5 meteorological reanalysis to monitor storm dynamics. High-frequency (>30 Hz) seismic  
24 signals captured precipitation, while microseismic bands (0.1-1Hz) reflected wave-induced ground  
25 motion. [Analysis of infrasound data via unsupervised learning delineated periods of acoustic](#)  
26 [quiescence from storm-related activity. The temporal evolution of these infrasound states](#)  
27 [coincided with distinct patterns in seismic ground motion, suggesting a shared origin in the storm's](#)  
28 [atmospheric dynamics. ~~Infrasound data, analyzed using unsupervised learning, revealed distinct~~  
29 ~~storm phases and showed strong spectral correlation with recorded ground motion, pointing to~~  
30 ~~coupled atmosphere-lithosphere processes induced by the storm.~~ The infrasound array also  
31 detected over 1,100 signals in the 0.6-7 Hz band, matching lightning discharges observed by  
32 geostationary satellites. ~~GNSS-derived estimates of precipitable water vapor tracked atmospheric~~  
33 ~~moisture buildup and showed clear correlation with intense rainfall, including potential precursory~~  
34 ~~signals days before peak precipitation.~~ \[GNSS data recorded a buildup of precipitable water vapor\]\(#\)  
35 \[that peaked concurrently with intense rainfall, following a multi-day increase that preceded the\]\(#\)  
36 \[main storm phase.\]\(#\) This study highlights the value of integrating diverse, non-traditional datasets  
37 to enhance the resolution and depth of storm analysis. Their combined use offers a more holistic  
38 understanding of storm evolution and supports the development of improved early-warning  
39 systems in vulnerable coastal regions.](#)

40 **Graphical abstract**

41



42

43

44

45

46

47

48

49

50

## 51 **1. Introduction**

52 Climate change has become a critical global issue, with far-reaching effects on weather patterns  
53 and the frequency and intensity of extreme events (Stott, 2016). These changes are not only  
54 contributing to more severe weather events but also altering the timing, location, and duration of  
55 storms, making them harder to predict and manage (Bengtsson et al., 2006). Understanding how  
56 to effectively monitor and predict the behavior of storms, particularly extreme ones, is crucial for  
57 improving forecasting models, enhancing early warning systems, and mitigating their impacts on  
58 both natural and human systems.

59 Traditional meteorological monitoring relies heavily on ground-based stations, weather radars, and  
60 satellite observations to track and predict storm behavior (Kober and Tafferner, 2009). These  
61 systems have been the backbone of weather forecasting for decades, providing valuable data on  
62 temperature, pressure, wind speed, and precipitation. However, while these methods are effective,  
63 they often have limitations in terms of spatial coverage (e.g. Sokol et al., 2021), particularly in  
64 remote or hard-to-reach areas. Additionally, they may struggle to capture certain atmospheric  
65 phenomena in real-time. As a result, non-conventional monitoring methods are increasingly being  
66 integrated into storm tracking efforts to complement existing meteorological approaches (e.g. Bosy  
67 et al., 2012; Burtin et al., 2016; Diaz et al., 2023; Coviello et al., 2024) .

68 In this context, our study focuses on the integration of alternative environmental datasets, including  
69 GNSS stations, infrasound sensors, and seismic data, to track the dynamics of an extreme storm  
70 event, as part of a national climate change resilience strategy, implemented through the DTE  
71 Climate project (<https://dteclimate.upb.ro/>). GNSS data provide valuable information on  
72 atmospheric water vapor, helping to track moisture changes that influence storm formation and  
73 intensity (Bosy et al, 2012; Marut et al., 2022). Infrasound sensors detect low-frequency acoustic  
74 waves generated by storm activity, such as lightning or large-scale weather system movements  
75 like microbaroms (e.g. Landès et al., 2012). Seismic data, though traditionally used for earthquake  
76 monitoring, can also record vibrations caused by storm-induced pressure changes, making it useful  
77 for detecting rainstorms, floods, or tropical cyclones (e.g. Retailleau and Gualtieri, 2021). Through  
78 the integration of these diverse sensor networks, our work highlights their synergy in improving  
79 storm detection, monitoring capabilities, and early warning systems, contributing to more robust  
80 climate resilience strategies.

81

82

83

84

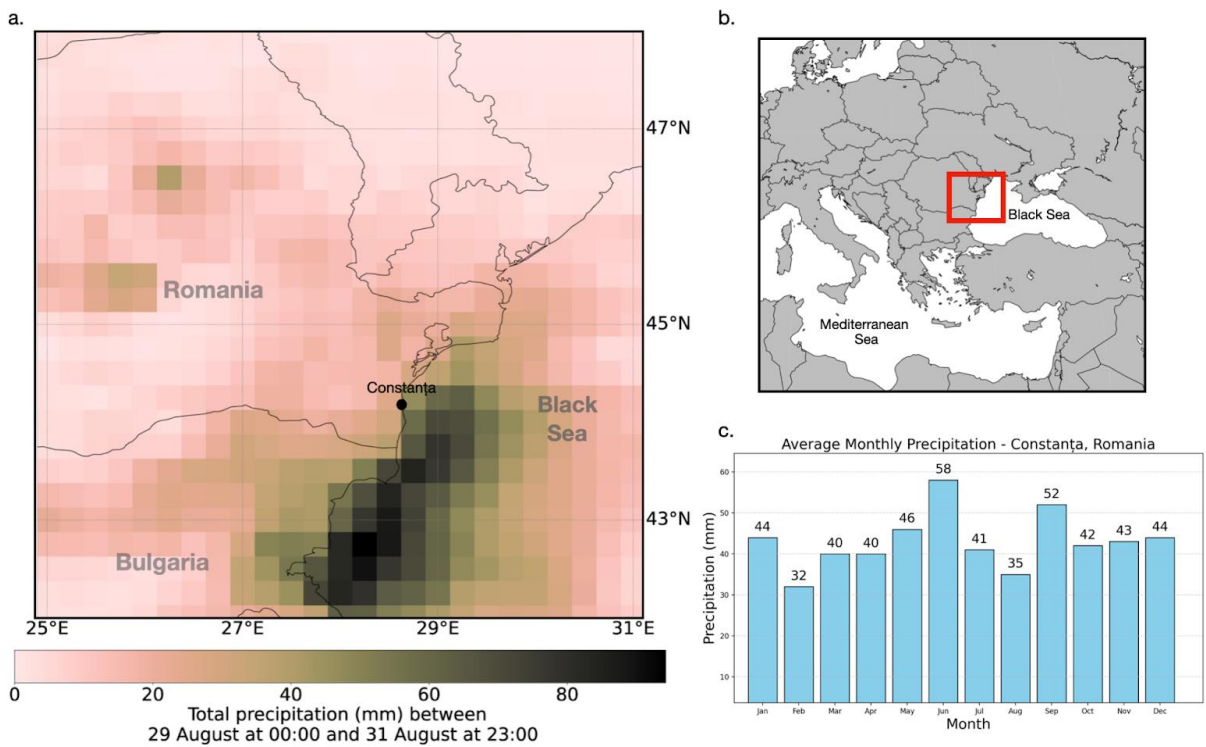
85

86

## 88 2. Study area and storm overview

89

90 The Black Sea region (Figure 1) is characterized by a unique combination of geographic and  
 91 meteorological features that significantly influence its climate and weather patterns. Nestled  
 92 between Europe and Asia, the Black Sea is bordered by six countries with diverse landscapes, from  
 93 mountainous areas to flat plains. This geography, combined with the Black Sea's relatively shallow  
 94 waters compared to oceanic environments and its connection to the Mediterranean through the  
 95 Bosphorus Strait, creates an environment where rapid changes in weather are common.  
 96 Understanding the dynamics of these extreme weather events is crucial, as they can have a  
 97 profound impact on the environment, economy, and daily life in the region. Monitoring such events  
 98 is key to improving our ability to predict their occurrence and intensity. By studying the complex  
 99 atmospheric processes that govern these storms, we can enhance predictive models and refine early  
 100 warning systems, ultimately helping to mitigate the risks and protect the communities and  
 101 ecosystems most vulnerable to these extreme weather phenomena.



102

103 *Figure 1. a. Total precipitation accumulated (in mm, shaded according to the scale) between 29*  
 104 *August 00 UTC and 31 August 23:00 UTC extracted from ERA5 data. The positions of the seismic*  
 105 *stations in eastern Romania are also indicated; b. Map of Europe with red square marking the*  
 106 *study region; c. Average monthly precipitation rates in Constanța, Romania.*

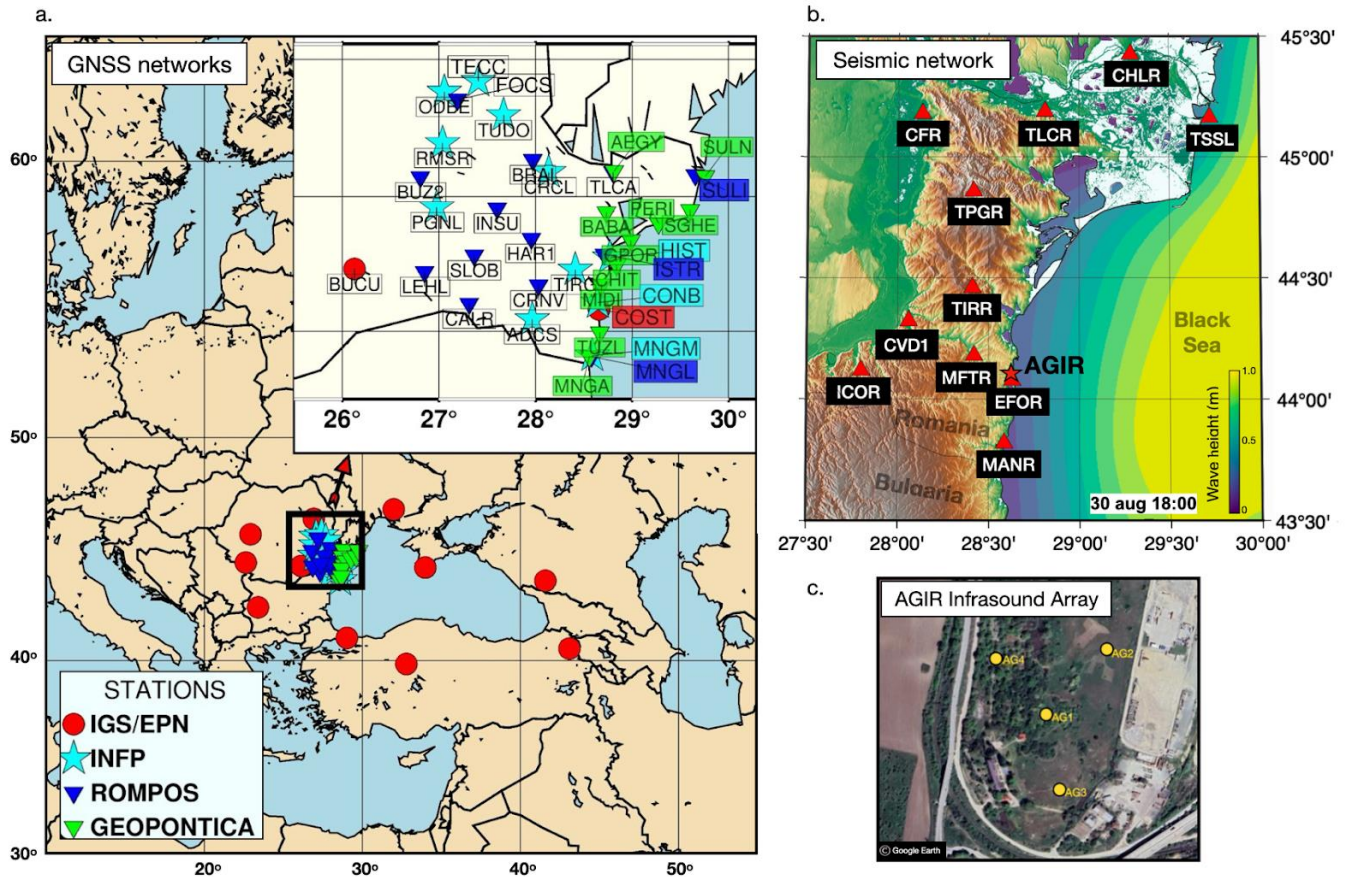
107 In August 2024, Romania experienced severe flooding, largely driven by a storm that brought  
 108 unusual precipitation patterns to the Black Sea coastal region. Exceptional precipitation totals were

109 recorded over south-eastern Romania in particular in Mangalia (225.9234.7 mm), Agigea (145  
110 mm), and Tuzla (118 mm), leading to significant flooding in coastal towns (Figure 1). Over 800  
111 emergency calls prompted large-scale intervention by ISU Dobrogea, focusing on evacuations,  
112 debris clearance, and infrastructure restoration (Antonescu et al. 2024). According to the National  
113 Meteorological Agency official records ([https://www.meteoromania.ro/clim/caracterizare-](https://www.meteoromania.ro/clim/caracterizare-lunara/cc_2024_08.html)  
114 [lunara/cc\\_2024\\_08.html](https://www.meteoromania.ro/clim/caracterizare-lunara/cc_2024_08.html)), one of the coastal stations at Mangalia, recorded a total of 343.6 mm of  
115 precipitation in August 2024, breaking the previous record of 159.1 mm from 1947, and  
116 significantly surpassing the average monthly precipitation values for this area (Figure 1c). A  
117 remarkable 234.7 mm of this total fell in a single day on August 31, 2024, highlighting the event's  
118 exceptional intensity.

119 An analysis conducted by ClimaMeter ([www.climameter.org](http://www.climameter.org), Faranda et al. 2024, Antonescu et  
120 al. 2024) immediately after the event, showed that low pressure systems similar to the one that  
121 caused the floods typically result in reduced rainfall (7 mm day<sup>-1</sup>, or up to 15% less) in eastern  
122 Romania compared to historical trends. However, this particular storm led to a significant local  
123 increase in precipitation, particularly in Constanța, one of the coastal cities severely affected by  
124 the flooding. In Constanța, daily rainfall reached up to 5 mm day<sup>-1</sup>, or up to 10% more than usual,  
125 marking a notable deviation from the region's typical weather behavior. The changes in  
126 precipitation that contributed to the flooding are largely attributed to human-induced climate  
127 change, with natural climate variability likely playing a modest role. As climate change continues  
128 to influence weather patterns, understanding the connection between changing precipitation levels  
129 and extreme weather events like flooding is crucial for improving forecasting and resilience in the  
130 face of such disasters.

### 131 **3. Data and Methods**

132 The analysis of the storm event integrates a variety of data sources and methodologies to provide  
133 a comprehensive understanding of its dynamics. Seismic data, infrasound measurements, GNSS  
134 water vapor data, and ERA5 reanalysis data are all utilized to capture different aspects of the  
135 storm's behavior (Figure 2). Seismic data offers insights into ground vibrations and atmospheric  
136 disturbances, while infrasound monitoring detects low-frequency acoustic signals generated by  
137 lightning and other meteorological phenomena. GNSS water vapor data provides valuable  
138 information on atmospheric moisture. Additionally, ERA5 reanalysis data (Hersbach et al. 2020),  
139 which provides detailed atmospheric and wave dynamics data, helps contextualize the storm's  
140 impact within broader weather patterns. Together, these diverse data sources enable a multifaceted  
141 approach to studying the storm and its effects.



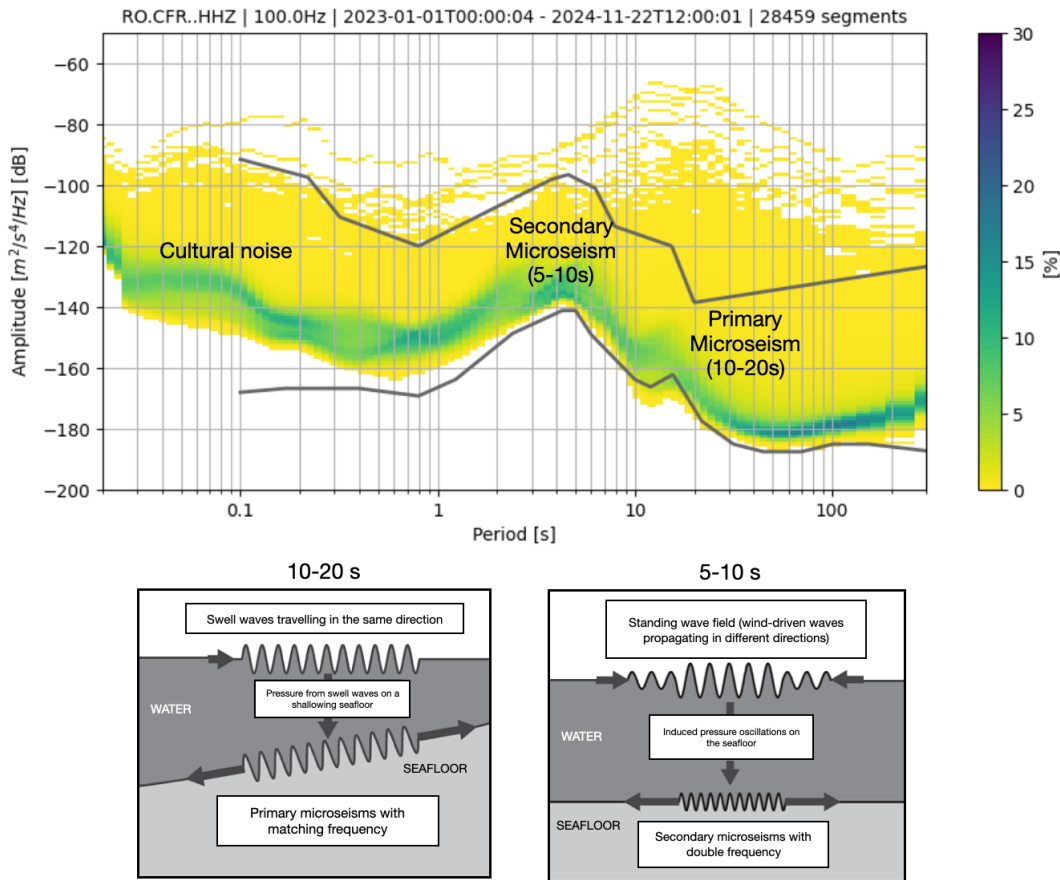
142  
 143 **Figure 2.** a. Map of Europe and the Black Sea coast showing GNSS stations and their belonging  
 144 networks used for analysis in this study. b. Map of the Romanian sea coast showing seismic stations (red  
 145 triangles) and the location of the AGIR infrasound array (star). Coloured contours represent total wave  
 146 height at 18:00 on the 30th of August 2024 from ERA5 reanalysis data. c. The layout of the AGIR infrasound  
 147 array.

### 148 3.1 Seismic Data

149 Seismic data represents vibrations of the Earth's surface, commonly referred to as seismic noise.  
 150 These low-amplitude movements are recorded across the Earth's surface and are traditionally used  
 151 to study the Earth's internal structure and detect earthquakes. Recently, it has increasingly found  
 152 applications in meteorology and hydrology, particularly for monitoring weather events (e.g. Dias  
 153 et al. 2023; Hua et al., 2023), destructive flood episodes (Burtin et al., 2016), ocean storms, and  
 154 tropical cyclones (Gualtieri et al., 2018). Seismic noise can reveal the impact of atmospheric and  
 155 oceanic conditions, providing valuable insights into weather events and climate changes (e.g.  
 156 Bromirski et al. 2002; Aster et al, 2008; 2023). In particular, seismic data helps track variations  
 157 in the Earth's surface caused by factors such as ocean waves, wind, and precipitation, offering a  
 158 unique perspective on these phenomena (e.g. Grevemeyer et al., 2000; Borzi et al., 2022).

159 When the seismic noise is analyzed in the frequency domain, two clear peaks emerge in the  
 160 spectrum (Figure 3), reflecting distinct types of seismic data also reveals two primary peaks  
 161 (Figure 3) related to ocean wave interactions (Koper et al., 2015; Ardhuin et al., 2019; Tanimoto

162 et al., 2023). The primary peak, observed in the range of 10-20 seconds (0.05-1 Hz), is generated  
 163 by the impact of "swell" waves traveling in the same direction, inducing pressure variations in the  
 164 Earth's crust that match the period of the waves. The secondary peak, in the range of 5-10 seconds  
 165 (0.1-0.5 Hz), is produced by wind-driven waves, which propagate in different directions and  
 166 generate pressure oscillations on the ocean floor (Ebeling et al., 2012). These seismic signals  
 167 directly link ocean conditions with seismic activity (Li et al., 2020), providing insights into large-  
 168 scale weather phenomena like ocean storms.



169  
 170 *Figure 3. Probabilistic Power Spectral Density (PPSD) of seismic noise for station CFR, over two years,*  
 171 *showing key sources of primary and secondary microseisms. Below, sketches illustrate the generation*  
 172 *mechanisms: primary microseisms are caused by unidirectional swell waves inducing pressure fluctuations*  
 173 *on a shoaling seafloor, while secondary microseisms result from nonlinear interactions of wind-driven*  
 174 *waves over deeper water (modified after Ebeling, 2012).*

175 Higher frequencies above 30 Hz are associated with the effects of precipitation and wind, as seen  
 176 in studies like Rindraharisaona et al. (2022) or Diaz et al. (2023). These higher-frequency seismic  
 177 signals help track more localized weather events, such as storms and heavy rainfall. Seismic data,  
 178 when integrated with other meteorological tools, enhances the ability to monitor and predict  
 179 weather events.

180 To analyse seismic data, the raw traces are first corrected for instrument response and converted  
181 to units of velocity. These are then filtered with [bandpass](#) butterworth filters adapted to capture the  
182 target signal: low pass filtering (<1 Hz) for wave-seafloor coupled interactions and high pass  
183 filtering (>30 Hz) to identify possible signatures of precipitation, essentially induced pressure  
184 fluctuations in the ground converted to weak seismic vibrations due to rain drops. Spectrograms  
185 of these filtered seismic traces [were computed using short-time Fourier transforms implemented](#)  
186 [in the scipy.signal package, with the default 256-sample window length used for each segment,](#)  
187 ~~are also used~~ to visualise signatures of the hydro-meteorological phenomena in the frequency  
188 content of ground vibrations.

189 Potential environmental signals in the seismic data were also investigated using power spectral  
190 density (PSD) analysis. To account for variations over time, a Probabilistic Power Spectral Density  
191 (PPSD) method was applied. [The continuous waveform was divided into 1-hour time windows](#)  
192 [with 50% overlap, and a PSD was computed for each window after instrument-response correction](#)  
193 [and basic preprocessing. These estimates were combined into a probability distribution, providing](#)  
194 [a statistical overview of typical and transient noise levels across frequencies. This approach](#)  
195 ~~combines PSD estimates from overlapping time windows into a probability distribution, providing~~  
196 ~~a comprehensive view of the range and likelihood of noise levels at different frequencies. Typical~~  
197 ~~noise conditions, as well as transient or extreme events, are captured in this analysis. To compute~~  
198 The PPSD was produced using ObsPy ~~was used~~ (Beyreuther et al., 2010), which handles data gaps  
199 and ensures reliable normalization.

200 Temporal variations in PSD amplitudes are also analyzed to track changes in seismic noise at  
201 specific frequencies. By extracting PSD values at selected frequencies that are expected to capture  
202 primary and secondary microseisms, time series of noise levels are generated. These temporal  
203 PSDs allow for the identification of trends and correlations with environmental factors, such as  
204 ocean wave activity or weather conditions.

## 205 **3.2 Acoustic Data**

206 Infrasound waves are low-frequency acoustic waves that are inaudible to the human ear, typically  
207 below 20 Hz. These waves are generated by a variety of natural and anthropogenic sources,  
208 including meteorological events, volcanic eruptions, earthquakes, and human activities such as  
209 explosions and industrial processes (Campus, 2009; Bondár et al., 2022). In particular, infrasound  
210 is often associated with phenomena like thunderstorms, ocean waves, and large-scale atmospheric  
211 events, which generate pressure fluctuations that propagate through the atmosphere (e.g. Stopa et  
212 al., 2012; Landès et al., 2012; Listowski et al., 2022). These waves provide valuable information  
213 about the dynamics of weather systems (e.g. Hupe et al., 2019), making them an essential tool for  
214 monitoring and understanding environmental processes (e.g. Brachet et al., 2009; Hupe et al.,  
215 2022). [Infrasound associated with thunderstorms, primarily generated by acoustic waves from](#)  
216 [thunder, has been studied previously and shown to be detectable at distances ranging from tens to](#)  
217 [hundreds of kilometers \(e.g., Assink et al., 2008; Sindelarova et al., 2015; Šindelářová et al., 2021\).](#)  
218 [Nevertheless, infrasound arrays detect signals from multiple storm-related sources, not just thunder](#)  
219 [\(e.g., Waxler et al., 2024\). In the present study, we build on this understanding by integrating these](#)  
220 [signals with seismic, satellite, meteorological, and water vapor observations to investigate what](#)  
221 [these complementary datasets reveal about storm evolution in a coastal environment.](#)

222 For the monitoring of infrasound signals, we use data from an infrasound array system located at  
223 Eforie Nord-Agigea, Romania (AGIR, Figure 2). This array consists of multiple sensors, including  
224 SIS-1 infrasonic sensors (Seismowave), equipped with global positioning systems (GPS) and noise  
225 reduction technology.

226 To analyze the seismo-acoustic characteristics of the August 30-31 Black Sea storm, we used a  
227 two-pronged approach: (1) single-station signal analysis based on feature extraction and  
228 unsupervised machine learning, and (2) array-based analysis using classic multi-channel  
229 correlation algorithms. Together, these methods provide complementary insights into the acoustic  
230 behavior of the storm, capturing both local signal characteristics and spatial coherence across  
231 sensors.

232 For the single-station analysis, infrasound data recorded at the AGIR sensor (Figure 2) was  
233 segmented into 30-minute windows, and a set of time-frequency features was extracted to  
234 characterize the signal dynamics. These features describe how energy and frequency content  
235 evolve over time, providing insights into the structure of the infrasound signal. ~~Parameters such as~~  
236 ~~spectral centroid and spectral rolloff are standard descriptors in acoustic signal analysis and are~~  
237 ~~suitable here because they effectively capture shifts in dominant frequency produced by lightning-~~  
238 ~~generated acoustic waves or the passage of pressure disturbances, while spectral flux highlights~~  
239 ~~changes in broadband acoustic energy (Pásztor et al., 2023). Spectral entropy reflects the~~  
240 ~~complexity of the frequency distribution, which increases during turbulent atmospheric conditions,~~  
241 ~~and the zero-crossing rate, mean, and variance of the power spectrum summarize overall activity~~  
242 ~~and variability. This feature set provides a compact representation of the signal suitable for~~  
243 ~~unsupervised machine-learning approaches such as clustering, techniques widely used in data~~  
244 ~~mining to identify patterns in multidimensional time–frequency data (e.g., Coates and Ng, 2012),~~  
245 ~~and allows us to distinguish physically interpretable stages of storm-induced changes in the~~  
246 ~~infrasound wavefield. The spectral centroid, spectral flux, spectral rolloff, and spectral entropy~~  
247 ~~capture various aspects of the frequency distribution and its complexity, while the zero-crossing~~  
248 ~~rate, mean, and variance of the power spectrum reflect signal activity and variability. These~~  
249 ~~features together form a multidimensional representation of the infrasound signal during the storm.~~

250 The extracted features were used as input for K-Means clustering (MacQueen, 1967), an  
251 unsupervised machine learning algorithm that partitions data into a predefined number of groups,  
252 in this case, seven. K-Means minimizes within-cluster variance by iteratively assigning feature  
253 vectors to the nearest cluster centroid and updating the centroids based on the grouped data. This  
254 clustering method enables the identification of distinct acoustic patterns in the signal (e.g. Pásztor  
255 et al., 2023), offering a data-driven way to segment the storm’s infrasound profile without  
256 requiring prior labels or assumptions. ~~The optimal number of clusters was determined using the~~  
257 ~~elbow method, which evaluates within-cluster variance as a function of cluster number. To select~~  
258 ~~the most informative features, we applied covariance pruning, and the temporal evolution of the~~  
259 ~~features was visualized to ensure meaningful representation. This procedure resulted in six~~  
260 ~~clusters, providing a balanced representation of the infrasound dynamics while avoiding over-~~  
261 ~~segmentation or overfitting. By combining multiple features in the clustering, this method captures~~  
262 ~~the evolving acoustic states of the storm in a compact, interpretable form.~~

263 In parallel with the single-station analysis, we also applied the Progressive Multi-Channel  
264 Correlation (PMCC) method, ~~as implemented in the DTK-PMCC software~~ (Cansi and Le Pichon,

265 2008; Le Pichon et al., 2010) to detect and analyze coherent acoustic signals across an infrasound  
266 array. The PMCC method targets signals generated by atmospheric sources such as lightning (i.e.,  
267 associated thunders) or other pressure disturbances, operating in the low-frequency range of 0.7 to  
268 7 Hz. It is specifically suited for mini-array configurations, where signal coherence between  
269 closely spaced sensors can be exploited for precise signal detection and characterization.

270 The PMCC algorithm divides waveform recordings into overlapping time windows and processes  
271 them across logarithmically spaced frequency bands. was implemented using a multi-resolution  
272 configuration following the standardization proposed by Garcés (2013), with window lengths and  
273 frequency bands arranged in third-octave bands. A total of 19 frequency bands were used, covering  
274 0.1-7 Hz. Window lengths decrease logarithmically with frequency, ranging from 258 s in the  
275 lowest band to 4 s in the highest band. A 10% time step was applied (corresponding to 90% overlap  
276 between consecutive windows), and this scheme repeats every decade.

277 Within each time-frequency segment, cross-correlations are computed between all sensor pairs to  
278 identify coherent wavefronts, signals that exhibit consistent arrival times across the array. From  
279 these detections, PMCC estimates several key propagation parameters, including back-azimuth  
280 (the direction of arrival), horizontal trace velocity, amplitude, duration, and dominant frequency.  
281 This approach is particularly effective in noisy environments and enables the discrimination of  
282 storm-generated infrasound from background signals or unrelated acoustic sources. The  
283 algorithm's output consists of a time-frequency map of signal detections enriched with physical  
284 metadata, allowing for detailed interpretation of the storm's acoustic footprint and its temporal  
285 evolution.

### 286 3.3 Satellite Observations

287 We also incorporated data from the Meteosat Third Generation (MTG) satellite system (Holmlund  
288 et al., 2021), specifically from its Lightning Imager (LI) sensor (Vitichie et al., 2020). The MTG  
289 satellites operate in geostationary orbit at approximately 36,000 km altitude, providing continuous  
290 observations over Europe, Africa, and surrounding waters. The Lightning Imager detects cloud-  
291 to-cloud, cloud-to-ground, and intra-cloud lightning flashes using four cameras that collectively  
292 cover 86% of the Earth's visible disc from the satellite's perspective.

293 For this study, we used Level 2 group data, which includes the geographical coordinates and timing  
294 of each detected flash. By mapping these detections, we were able to analyze the spatial  
295 distribution and temporal evolution of the storm's lightning activity. The dataset also offered  
296 insights into the storm's intensity and structure, complementing other meteorological observations.

297 Associations between infrasound detections and lightning flashes detected by MTG within 50 km  
298 of the AGIR infrasound station were investigated by assuming direct-path acoustic propagation  
299 and a correspondence between infrasound time-of-arrival and the MTG lightning discharge time  
300 (after Assink et al., 2008):

$$301 t = t_{\text{MTG}} + d/c + \Delta t,$$

302 where  $d$  is the distance between the lightning discharge and the infrasound station,  $c = 340\text{m/s}$ ,  
303 and  $\Delta t = \pm 10\text{s}$  accounts for timing uncertainty. Additionally, a maximum angular deviation of

304 10° between the observed infrasound backazimuth and the MTG-derived backazimuth is permitted  
305 for an association to be accepted.

### 306 **3.4 GNSS Data**

307 The use of GNSS technology for atmospheric monitoring provides a powerful tool for analyzing  
308 extreme weather events. Beyond its well-known applications in navigation and timing, GNSS has  
309 become a reliable method for sensing tropospheric water vapour, an essential driver of weather  
310 systems and a key variable in forecasting models (Guerova et al., 2016; Vaquero-Martínez and  
311 Antón, 2021). Over the past two decades, ground-based GNSS networks in Europe have  
312 contributed significantly to operational meteorology by providing near real-time estimates of  
313 atmospheric water vapour, aiding in the detection and tracking of severe weather, including heavy  
314 rainfall and storms (Karabatić et al., 2011; Priego et al., 2017; Jones et al., 2020). These high-  
315 resolution observations have proven valuable for both nowcasting and validating numerical  
316 weather prediction models (Wilgan et al., 2015; Bosy et al., 2012; Awange, 2012).

317 In this study, GNSS data were collected from several networks (Figure 2), including the  
318 International GNSS Service (IGS, Johnston et al., 2017), the EUREF Permanent Network (EPN,  
319 Bruyninx et al., 2012), the Romanian Position Determination System (ROMPOS, Iliescu et al.,  
320 2019), and GEOPONTICA (Dimitriu et al., 2017). A total of 37 permanent GNSS stations were  
321 analyzed over a 30-day period, with the rainiest interval selected at the midpoint of the study  
322 period. These stations provide high-quality, continuous observations critical for atmospheric  
323 monitoring.

324 The data were processed using a double-differenced, ionosphere-free combination of L1 and L2  
325 carrier phases. This approach helps minimize errors such as ionospheric delays, satellite clock  
326 biases, and other common atmospheric effects. The resulting Zenith Tropospheric Delay (ZTD)  
327 values were then corrected using the Vienna Mapping Functions 3 (VMF3, Landskron et al., 2018),  
328 which improve the accuracy of ZTD by accounting for variations in the troposphere's atmospheric  
329 conditions. Once the ZTD was refined, it was converted into integrated precipitable water vapor  
330 (PWV) using surface meteorological data (temperature and pressure) from co-located weather  
331 stations, following the method outlined by Bosy et al. (2012). This process allowed for the  
332 derivation of high-resolution atmospheric water vapor content, critical for analyzing the dynamics  
333 of the extreme storm event over the Black Sea. By combining GNSS-derived PWV with data from  
334 other observational sources, the study captured the temporal and spatial variations in atmospheric  
335 moisture, offering valuable insights into the storm's development and intensity.

### 336 **3.5 Meteorological Data**

337 To compare the infrasound signals captured during the Black Sea extreme storm event, we  
338 extracted meteorological data from the open-access ERA5 reanalysis dataset, produced by the  
339 European Centre for Medium-Range Weather Forecasts (ECMWF). This dataset provides a  
340 comprehensive record of global weather conditions from 1950 to the present (Hersbach et al.,  
341 2023). ERA5 combines observational data and advanced numerical models to generate high-  
342 resolution atmospheric parameters, including precipitation (Figure 1), wind speed, and wave  
343 height. ERA5 has been extensively validated (Jiao et al., 2021; Wu et al., 2022; Soci et al., 2024)  
344 and is widely used in studies of storm evolution and precipitation dynamics (e.g. Dullart et al.,

345 2020; Tiberia et al., 2021; Price et al., 2025), making it a suitable choice for the mesoscale  
346 processes examined here.

347 For our study, the ERA5 data was used to track the meteorological context of the storm, offering  
348 insights into the intensity of precipitation, the evolution of wind patterns, and the development of  
349 oceanic wave heights. With high temporal (1 hour) and spatial ( $0.25^\circ \times 0.25^\circ$ ) resolution, ERA5  
350 allows for a detailed comparison of the storm's meteorological characteristics over time. These  
351 comparisons help us understand the storm's dynamics and assess its impact, further enhancing the  
352 interpretation of infrasound signals and aiding in future storm prediction and monitoring efforts.  
353 The open-access nature of ERA5 ensures broad accessibility, contributing to the transparency and  
354 reproducibility of our storm analysis (Copernicus Climate Change Service, Climate Data Store,  
355 2023).

## 356 4. Results

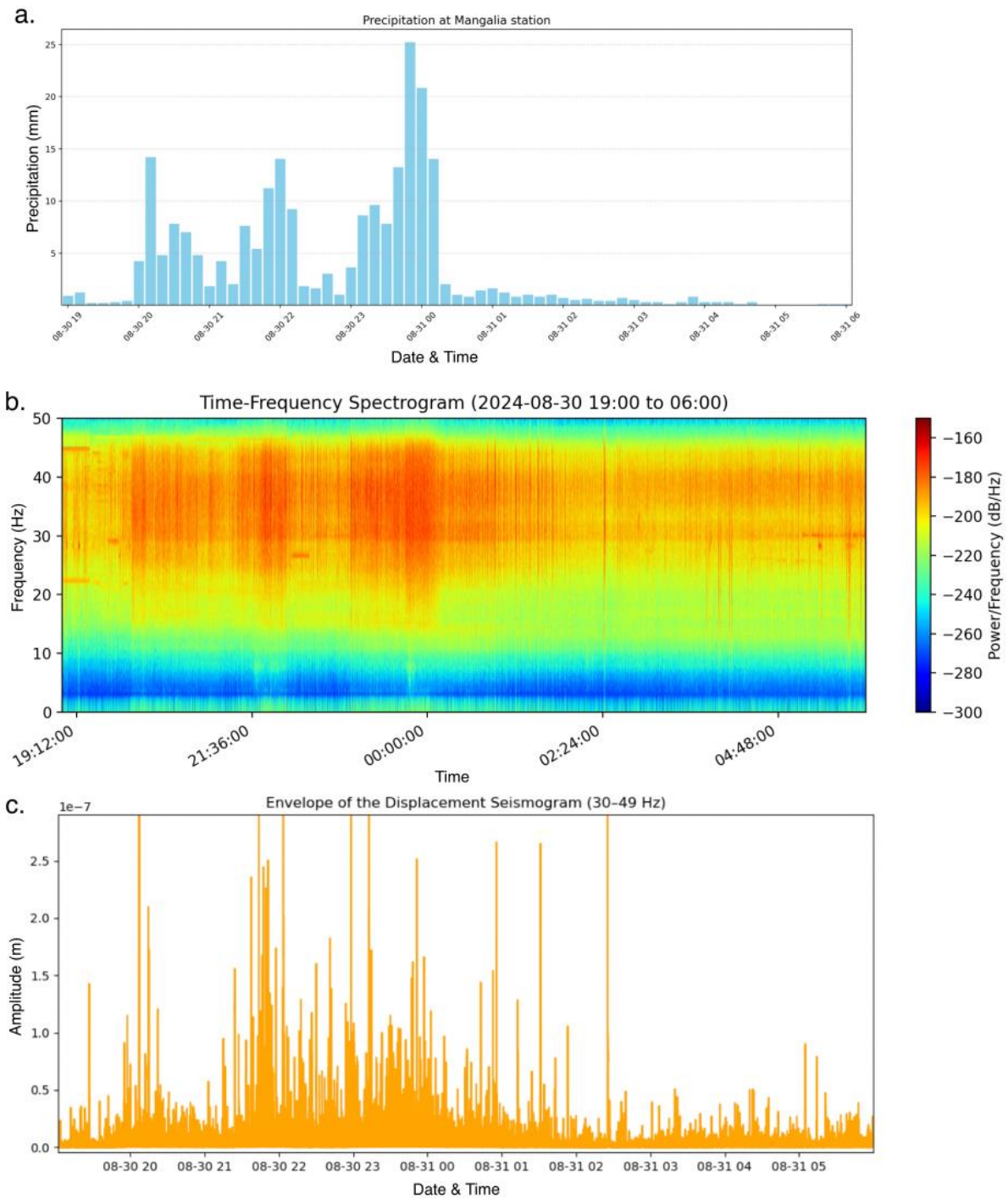
### 357 4.1 Seismic signatures of storm evolution

358 High frequency ( $>30$  Hz) analysis of seismic noise reveals strong signals during periods of intense  
359 rainfall at times when high precipitation values were also recorded (Figure 4). Specifically, an  
360 example of the velocity displacement envelope at station MANR and its spectrogram plotted for  
361 the period 30 August, 12:00 UTC to 31 August, 06:00 UTC 29th of august at 12 AM (00:00) to  
362 31st of August midnight UTC (Figures 4b,c) reveal strong signal around midnight the 18:00 UTC  
363 -00:00 UTC, when recorded most-precipitation exceeded 20 mm per 10 minutes. was estimated  
364 in the grid cell of the station (more than  $3 \text{ mm m}^{-2}$ , Figure 4a). Similar temporal patterns in the  
365 signatures and seismic spectrogram visualisations showed correlation were also visible when  
366 compared with hourly precipitation levels from ERA5, indicating that the high amplitude energy  
367 observed present on the high frequency velocity envelope and the time frequency spectrogram at  
368 frequencies above 30 Hz is most plausibly generated by raindrop impacts. likely caused by rain.  
369 Previous research showed a correlation with rain drop size as well (Rindraharisaona et al., 2022),  
370 although we did not have access to such information.

371 However, this correspondence is not uniform across all rainfall episodes. While the main  
372 precipitation maximum on 30-31 August produces a clear and sustained seismic response, several  
373 lower-intensity precipitation pulses show a much weaker or no recognizable signature in either the  
374 seismic envelope or spectrogram. This behaviour is consistent with previous work (e.g.,  
375 Rindraharisaona et al., 2022), which demonstrates that only rainfall above a certain intensity, or  
376 involving sufficiently large drops, generates impact forces strong enough to be detected by  
377 broadband seismometers. Our observations therefore reflect both strong positive correlations  
378 during intense rainfall and the lack of seismic expression for weaker precipitation. This selective  
379 sensitivity supports the interpretation that high-frequency seismic noise can reliably track strong  
380 rainfall peaks but is less responsive to light or moderate precipitation, an important nuance when  
381 interpreting multi-sensor relationships in this study.

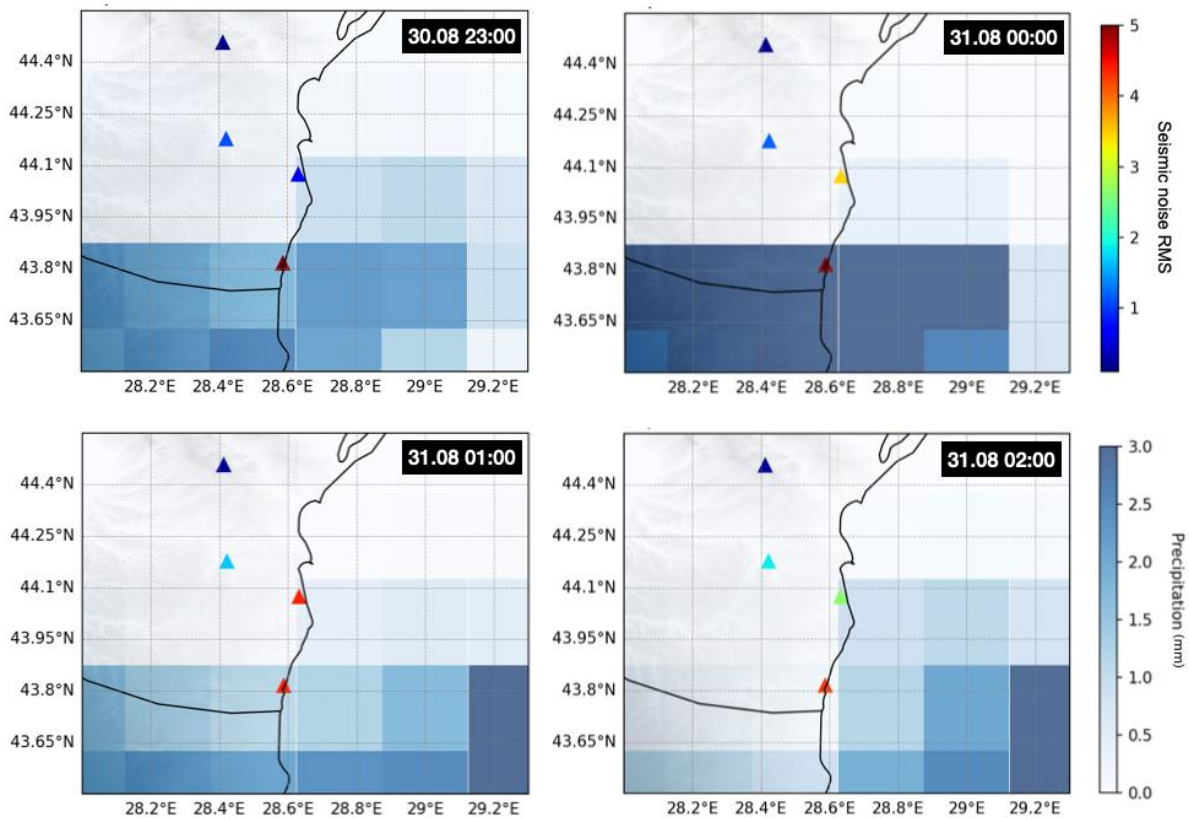
382 Anthropogenic seismic noise is typically strongest at low to mid frequencies ( $<25$  Hz), where day-  
383 night variations reflect traffic, human activity, and transient signals from machinery, while higher-  
384 frequency bands (25-45 Hz) may include periodic contributions from rotating equipment (e.g.,  
385 Gross & Ritter, 2008; Diaz et al., 2017). The bandwidth targeting rainfall in this case is between

386 30-50 Hz, which is above the dominant frequency content of most anthropogenic sources and  
 387 overlaps with raindrop-impact energy documented in recent rainfall-seismic studies.



388  
 389 *Figure 4. High frequency (30-50Hz) observations of the storm at station MANR. a. Time series of total*  
 390 *precipitation every 10 minutes from the ANM station at Mangalia per hour from ERA5 at the grid location*  
 391 *of station MANR. b. Spectrogram of the velocity seismic time series for station MANR. c. Envelope of the*  
 392 *velocity displacement seismogram at station MANR.*

393 To visualise the signature of the storm passing over the network of broadband seismic stations in  
 394 the coastal area, we also plotted the hourly precipitation values with the hourly root-mean-square  
 395 amplitudes of the high-frequency (>30 Hz) seismic velocity envelopes recorded at seismic stations.  
 396 Figure 5 shows three snapshots of hourly plots of gridded precipitation data from ERA5, which  
 397 have a lower amplitude than point measurements at the Mangalia station, due to the averaging over  
 398 the grid block. This figure illustrates a correlation presents a temporal coincidence between  
 399 changing precipitation patterns from ERA5 data and the amplitudes of high-frequency seismic  
 400 noise. This observation further supports the likelihood of a causal relationship. These high-  
 401 frequency seismic signals could potentially be monitored in near real time to flag intense rainfall  
 402 events, providing a conceptual basis for a simple streaming detection approach.

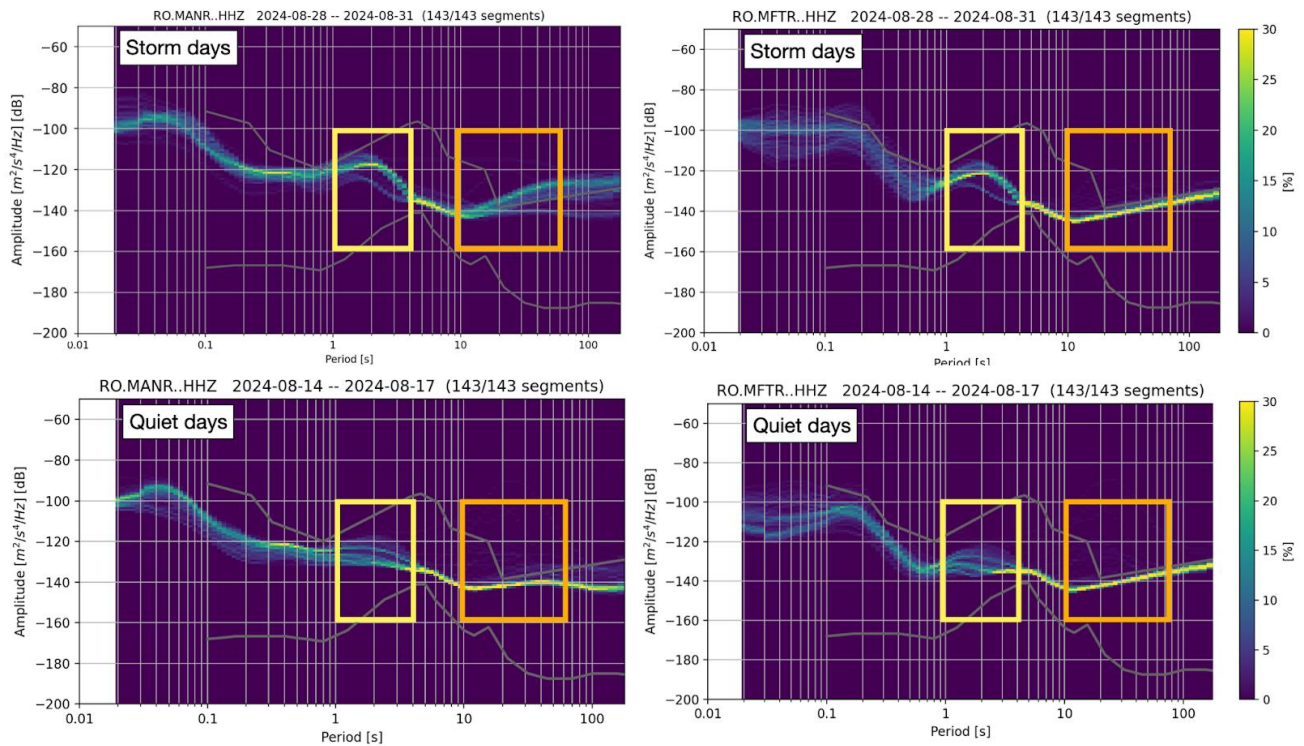


403  
 404 *Figure 5. Distribution of hourly RMS of high pass filtered (>30 Hz) seismograms and precipitation data.*  
 405 *Colours indicate hourly RMS amplitude of velocity envelopes filtered 30-50 Hz. Background coloured*  
 406 *grid indicates the total precipitation (mm) from ERA5 data.*

407 The analysis of the microseismic noise frequency band is closely linked to the interaction between  
 408 ocean waves and the seafloor, which is influenced by storm conditions. To assess the storm's  
 409 impact, we analyze the PPSD (Probabilistic Power Spectral Density) of noise recorded at several  
 410 stations during both storm and quiet days, using the latter as a baseline. Figure 6 shows examples  
 411 of PPSD at stations MANR and MFTR (Figure 2), revealing differences in PSD amplitudes across  
 412 the primary and secondary microseismic bands. These differences indicate the presence of high-  
 413 intensity wind-driven waves and swell energy in the sea.

414 The secondary microseismic band, in particular, shows a significant rise in amplitude during  
 415 storms, driven by wind-induced pressure fluctuations in the shoaling seafloor (Figure 3, Ebeling  
 416 et al., 2012). On quiet days, the PSD remains consistently lower, typically staying below the -120  
 417 dB threshold. This stark contrast emphasizes the role of atmospheric conditions in modulating  
 418 seismic noise, with storms causing a notable increase in energy across both frequency bands. The  
 419 temporal evolution of the PSD values (Figure 7) further highlights the storm's impact, with  
 420 fluctuations corresponding to changes in environmental factors, reinforcing the connection  
 421 between storm activity and the observed seismic signals.

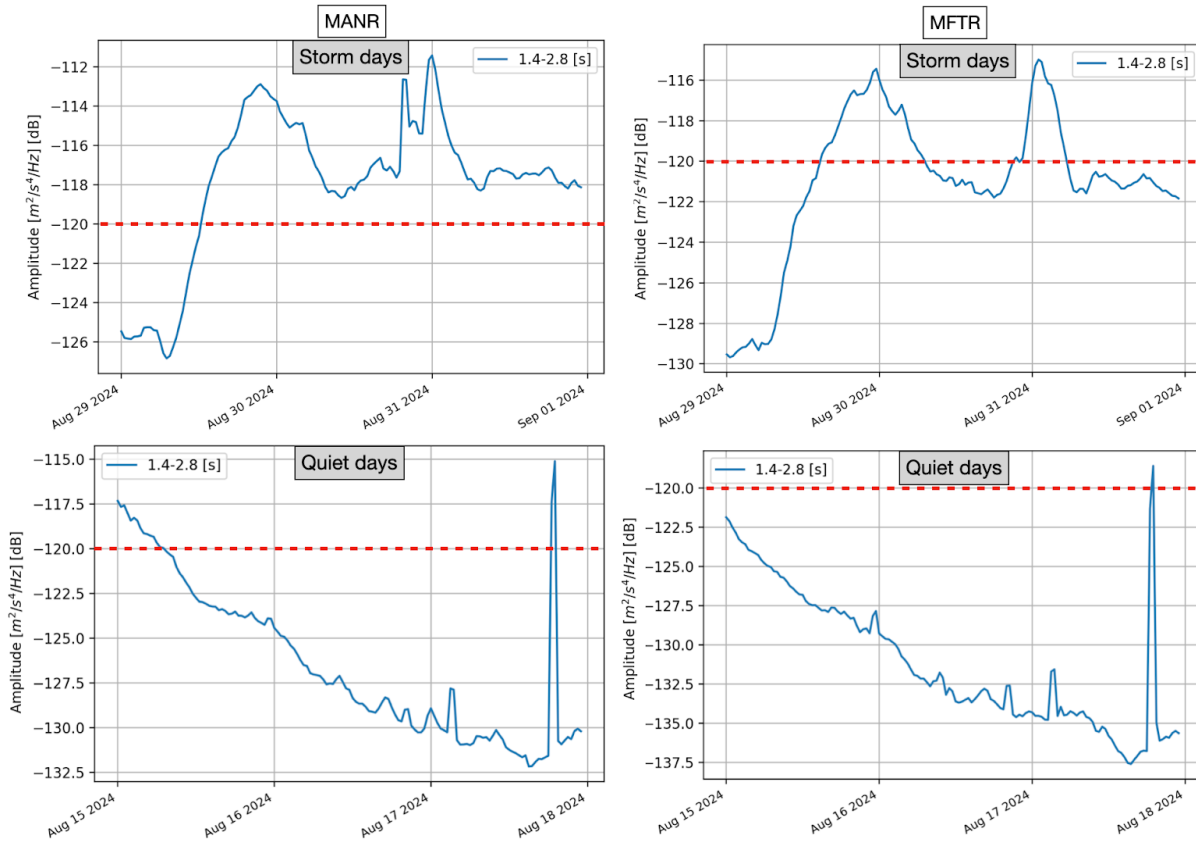
422



423

424 *Figure 6. Probabilistic Power Spectral Density (PPSD) plots for two seismic stations near the Black Sea*  
 425 *coast capturing the target storm signal in the microseismic bandwidths (marked with rectangles). The top*  
 426 *panels show the PPSD distributions across frequencies, indicating the probability of power spectral*  
 427 *density values in percentage for days including the Black Sea storm. The bottom panels show PPSD for*  
 428 *days with no recorded events.*

429 Anthropogenic seismic noise does not significantly affect the microseismic band (0.1-1 Hz).  
 430 Human-generated vibrations predominantly occupy frequencies above 1 Hz, while long-period  
 431 microseisms are produced by ocean wave interactions and are coherent over large distances. The  
 432 temporal evolution of the microseismic energy observed in this study matches changes in wave  
 433 state associated with the storm rather than any local activity. Similar to the findings of Gross &  
 434 Ritter (2009), the sub-Hz frequency range is dominated by natural sources, with anthropogenic  
 435 contributions being negligible.



436

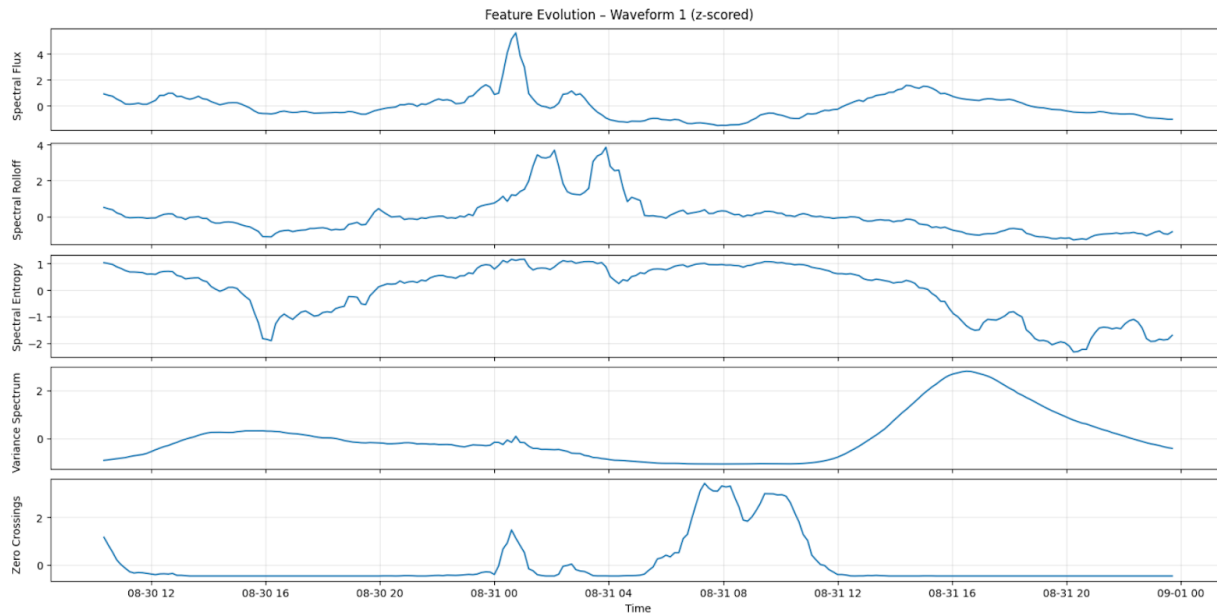
437 *Figure 7. Temporal PSDs for two seismic stations near the Black Sea Coast in the secondary*  
 438 *microseismic band showing significantly higher values ( $>-120$  dB) during stormy days compared to days*  
 439 *without recorded precipitation.*

#### 440 4.12 Infrasound and satellite lightning observations

##### 441 4.12.1 Single-station feature extraction

442 The evolution of time-frequency features over the duration of the Black Sea storm revealed distinct  
 443 patterns in the infrasound signal (Figures 8 and 9). Most features, including spectral flux, spectral  
 444 centroid, and spectral rolloff, exhibited a clear peak or a slightly bimodal peak corresponding to  
 445 the storm's peak intensity, indicating a strong relationship between these features and the storm's  
 446 dynamics. The peak in these features was most pronounced during the storm's active periods,  
 447 reflecting rapid changes in the atmospheric conditions. However, the zero-crossings feature did  
 448 not show a similarly distinct pattern, with its evolution being less evident in relation to the storm's  
 449 phases. This suggests that most spectral features are sensitive to storm-related acoustic shifts.  
 450 Centroid and rolloff show parallel behavior because they are both frequency-domain descriptors  
 451 tied to the distribution of spectral energy, and so both respond strongly to the same uplift in energy  
 452 during the storm's peak. Spectral flux, by contrast, quantifies inter-frame spectral change, so its  
 453 peak occurs where the spectrum transitions most rapidly, even when that does not coincide with  
 454 the maximum absolute energy (e.g. Pásztor et al., 2023). Finally, the zero-crossing rate reflects  
 455 time-domain volatility, not spectral shape, which explains its distinct pattern, such as the storm's

456 later stages may introduce broadband turbulence or noise components that boost zero crossings  
457 independently of the spectral shifts visible in the first two panels. While the individual features  
458 varied over time, it is the combination of these features through K-means clustering that effectively  
459 identifies the time frame corresponding to the main precipitation episode. Zero-crossings exhibited  
460 more variable patterns, reflecting high-frequency fluctuations, but the joint clustering of all  
461 features robustly captures the timing of the storm's most intense phases.

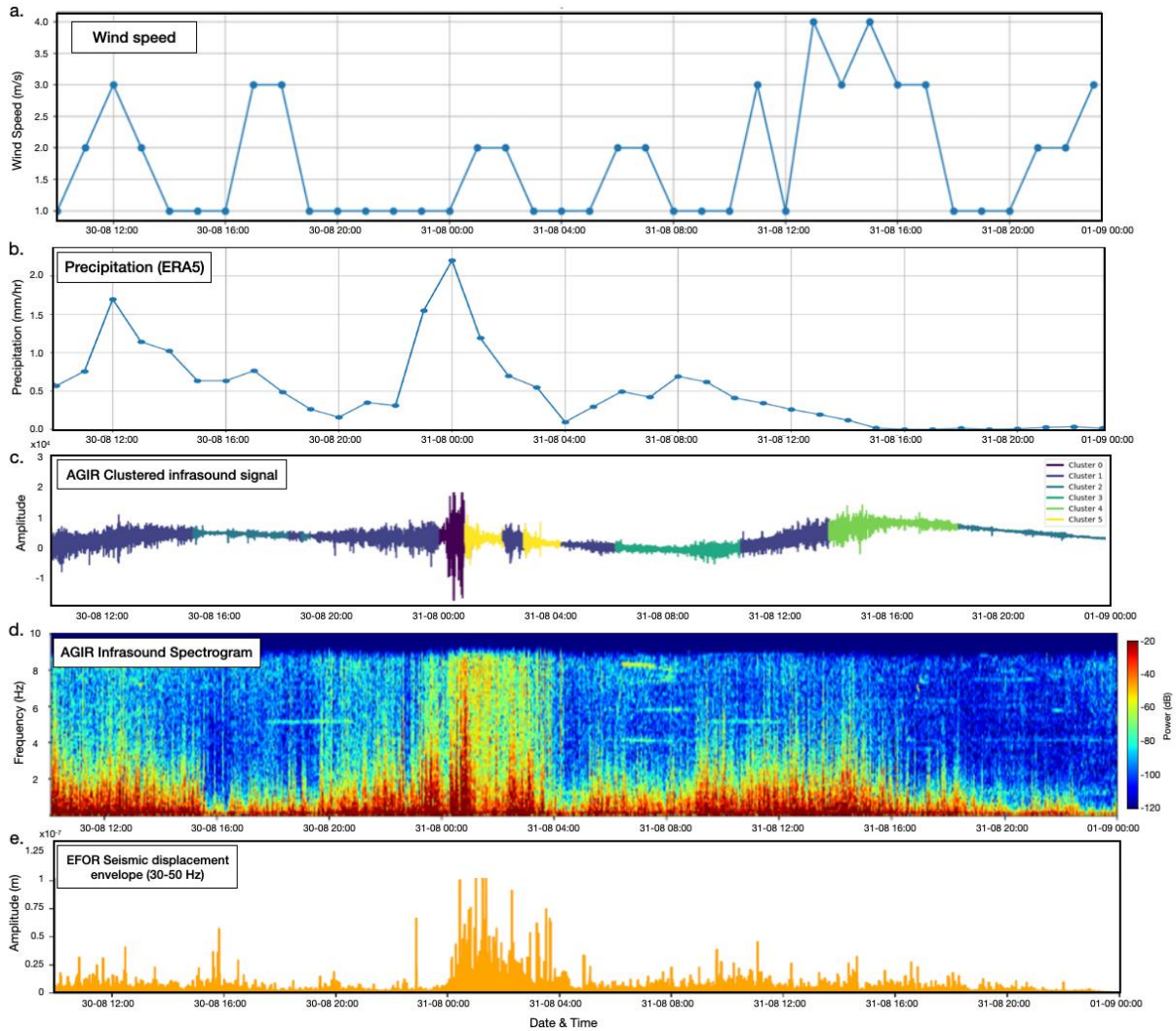


462

463 *Figure 8. Time-frequency feature analysis for the single-station infrasound signal recorded at AGIR during*  
464 *the Black Sea Storm.*

465 K-means clustering of the segmented infrasound signal, based on extracted time-frequency  
466 features, revealed the relationship between the storm's acoustic dynamics and its temporal  
467 evolution, using 7 clusters for the enhancement of both detection of storm phases and event  
468 detection. The segmented signal highlighted distinct phases of the storm, with each segment  
469 corresponding to clusters representing specific changes in spectral content. These segments  
470 exhibited clear matches with the storm's progression, indicating that the clustering technique  
471 effectively tracked variations in storm intensity and the corresponding acoustic features. Separated  
472 the acoustic data into six groups with distinct spectral and amplitude characteristics (Figure 9).  
473 These clusters highlight acoustic states that may relate to different environmental conditions  
474 during the monitoring period. For example, Cluster 0 coincides with periods of intense  
475 precipitation and stronger winds, while Cluster 1 captures intervals with moderate amplitudes but  
476 persistently elevated background acoustic levels, without corresponding rainfall or wind peaks.  
477 Cluster 2 reflects calmer conditions with low amplitudes and little or no precipitation. Transitional  
478 patterns also arise, such as Cluster 3, which appear before intervals grouped in Cluster 1 and mark  
479 intermediate acoustic activity. Overall, the clustering approach demonstrates that combining  
480 multiple features reveals consistent acoustic regimes and can help differentiate environmental  
481 conditions, without relying on any single parameter.

482 Interestingly, the spectral content of the infrasound signal showed similarities to seismic signal  
 483 envelopes, particularly in the high frequency ranges (Figure 9), which may suggest a connection  
 484 between the atmospheric pressure waves detected by infrasound and the ground vibrations  
 485 captured by seismic instruments. This overlap implies that both seismic and infrasound signals  
 486 could be complementary in capturing different aspects of storm dynamics, with seismic signals  
 487 reflecting ground vibrations and infrasound capturing the atmospheric processes.



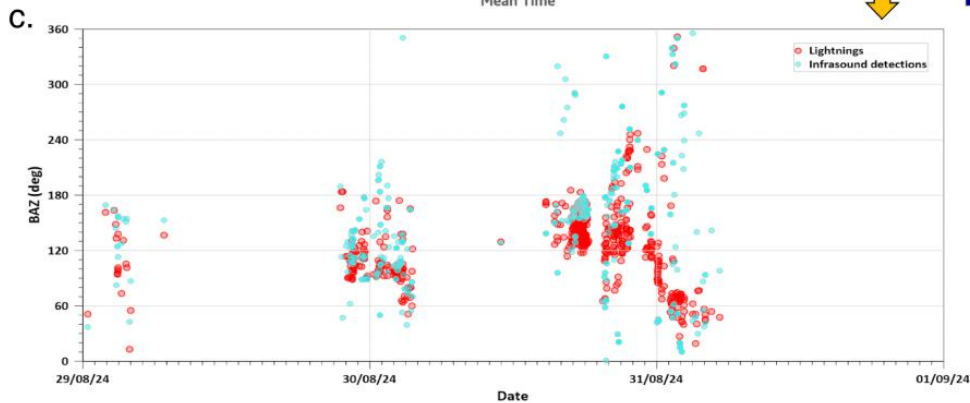
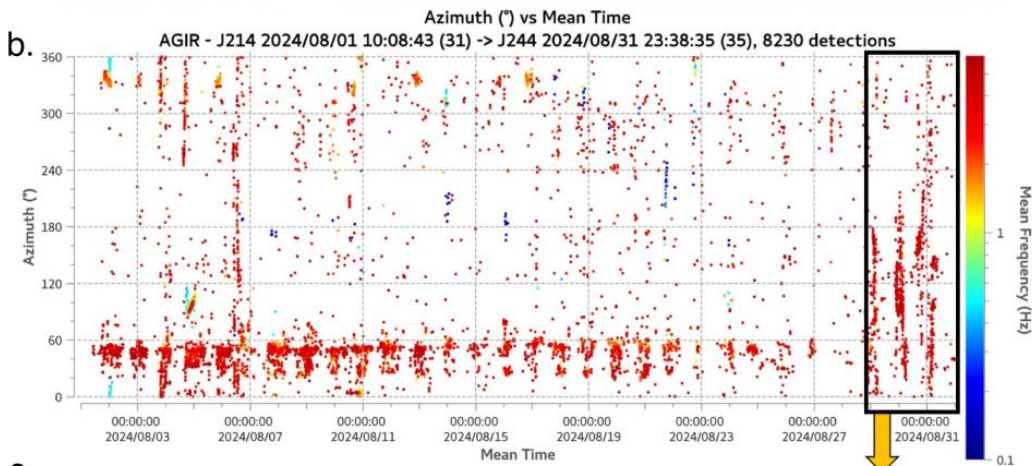
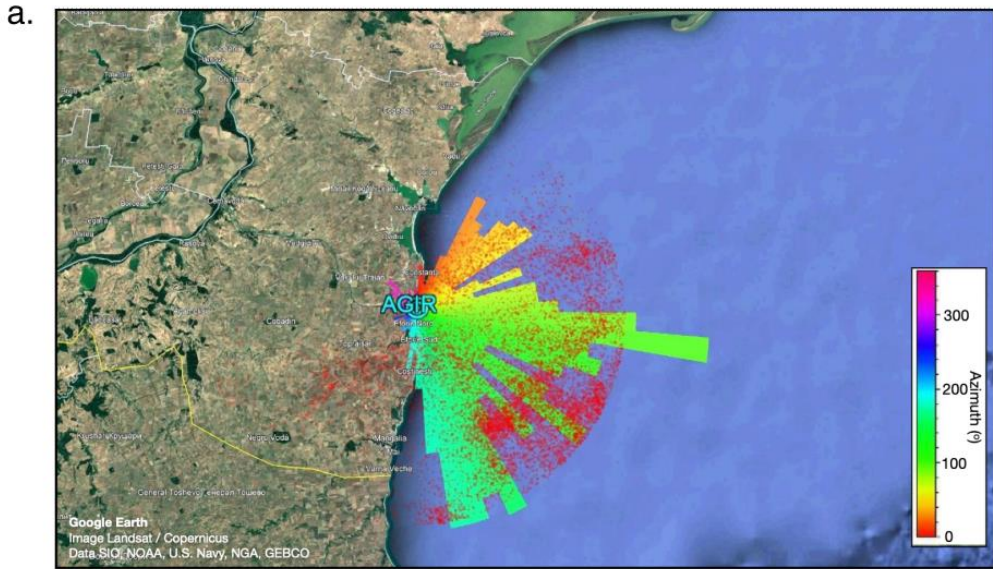
488  
 489 *Figure 9. Clustering results of infrasound signals recorded at AGIR from the August Black Sea storm event*  
 490 *compared with precipitation data and seismic signal from EFOR station. a. Wind speed per hour measured*  
 491 *at ANM meteorological station Constanta; b. Average precipitation data from 1°x1° around AGIR. c. Raw*  
 492 *infrasound signal recorded at the AGIR sensor during the period of August 30–31, 2024, with different*  
 493 *segments color-coded according to the cluster they belong to, based on K-means clustering of 30-minute*  
 494 *time-frequency feature windows. d. The corresponding spectrogram, generated using Blackman*  
 495 *windowing with 128 samples and 70% overlap; e. Seismic displacement envelope at station EFOR, filtered*  
 496 *between 30-50 Hz.*

497 **4.12.2 Array analysis and lightning detection**

498 The PMCC algorithm allowed us to isolate coherent infrasound signals and estimate their  
499 propagation parameters, such as back-azimuth and arrival times, across the sensor network. Nearly  
500 11,000 lightning flashes were detected by the MTG Lightning Imager within 50 km of the AGIR  
501 station during the Black Sea storm (Figure 10A), providing a dense reference set for comparison.  
502 Within the relevant 0.6-7 Hz frequency band, approximately 1,100 infrasound detections were  
503 identified. These signals primarily consisted of long-duration wave trains with frequent amplitude  
504 peaks and short-lived disturbances characteristic of lightning-generated infrasound. Their  
505 dominant frequency was around 3 Hz, and amplitudes ranged from 0.01 to 3.4 Pa (Figure 10b).

506 A subset of the infrasound detections could be confidently associated with individual lightning  
507 discharges based on temporal alignment and backazimuth consistency. Overall, we were able to  
508 associate 6.4% of lightning flashes with infrasound detections at AGIR (Figure 10c). This level of  
509 correspondence is reasonable given that only a subset of lightning discharges radiate infrasound  
510 efficiently and that propagation strongly depends on altitude, source geometry, and atmospheric  
511 conditions. Nevertheless, these coincident detections demonstrate that lightning-generated  
512 infrasound was clearly recorded during the storm and that the PMCC-derived acoustic signatures  
513 provide valuable insight into the evolution of electrical activity and storm dynamics. ~~These  
514 acoustic signatures, identified through the PMCC method, provide valuable insights into the  
515 storm's behavior, correlating infrasound signals with specific lightning events detected by the  
516 MTG Lightning Imager and enhancing our understanding of the atmospheric effects during the  
517 storm.~~

518 Anthropogenic noise sources, such as wind turbines (e.g., Jakobsen, 2005), industrial machinery  
519 (Gastmeier and Howe, 2008), and road traffic (Grafkina et al., 2019), are well-documented  
520 challenges for infrasound studies because they often generate persistent, periodic, or tonal signals  
521 that can mask natural atmospheric phenomena. The AGIR infrasound array used here is located in  
522 a semi-rural setting, distant from major roads and industrial facilities, which reduces the likelihood  
523 of local anthropogenic contamination. Several independent lines of evidence indicate that such  
524 contamination is negligible in this case study. First, the strongest infrasound signatures occurred  
525 during night-time hours, when human activity is minimal. Second, both the clustering and PMCC  
526 analyses identify transient signals with energy peaking around ~3 Hz, which contrasts sharply with  
527 the more continuous or harmonic spectral patterns typically produced by anthropogenic sources.  
528 Third, the temporal alignment of these acoustic signatures with independent observations of  
529 lightning and precipitation provides strong confirmation that the detected infrasound variability is  
530 storm-related rather than anthropogenic in origin.



531

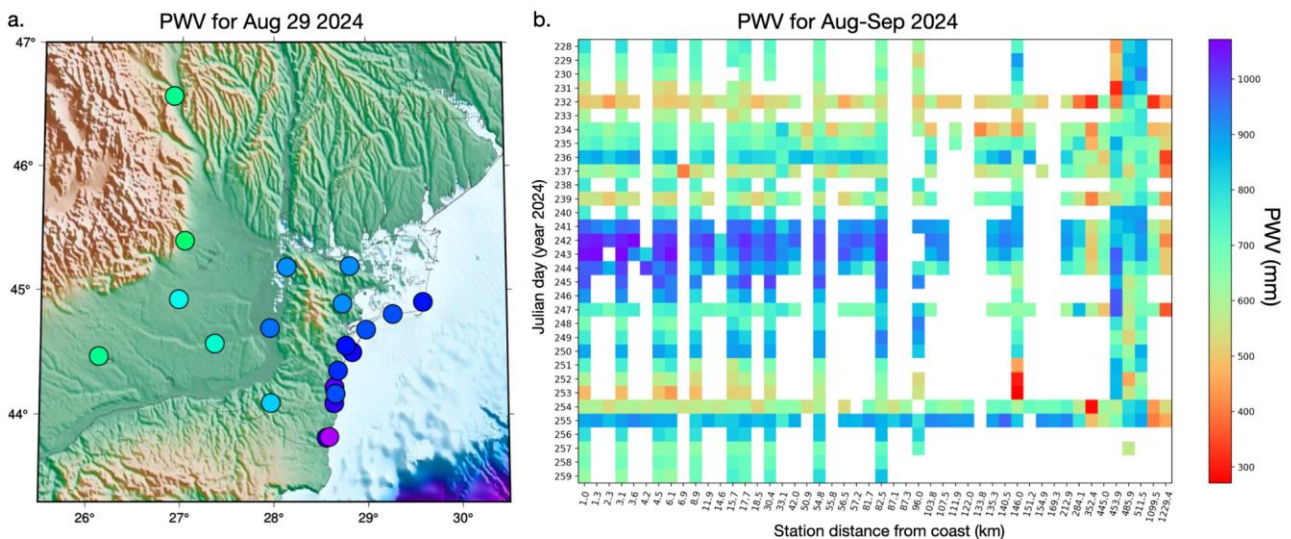
532 *Figure 10. a. Polar histogram of infrasound detections from the AGIR station, displayed with © Google*  
 533 *Earth, along with the locations of lightning strikes detected by the MTG Lightning Imager system for the*  
 534 *period from 29-31st of August 2024. The geographical position of the AGIR infrasound station is*  
 535 *also shown on the map. b. diagram of high-frequency detections from the AGIR infrasound station between*  
 536 *1-31st of August 2024 and 31, 2024. c. Associations between events detected by the AGIR infrasound array*  
 537 *and the MTG satellite database for 29-31st of August 2024.*

538  
539

### 4.3 GNSS-derived precipitable water vapor trends

540 The analysis of daily GNSS-derived precipitable water vapor (Figure 11) reveals clear temporal  
541 variations, with the highest PWV values consistently recorded on stormy days (>900 mm per day  
542 on DOY 240–243, i.e. August 27-30). Notably, the peak values occurred between DOY 241 and  
543 DOY 243 (Figure 11b), when the heaviest rainfall was observed (Figure 1). Coastal stations  
544 showed extremely high PWV values (>950 mm per day) compared to inland stations (>800 mm  
545 per day), with a slight decrease in PWV as we moved inland away from the coast (Figure 11a).  
546 This spatial distribution highlights the geographical gradient of atmospheric moisture, with the  
547 highest PWV concentrations near coastal areas, also decreasing gradually toward the north away  
548 from the storm peak. Interestingly, some inland stations (BUCU, PGNL, RMSR) recorded their  
549 peak PWV on DOY 255, corresponding to the onset of the Boris storm, another significant extreme  
550 rainfall event that swept through Central and Eastern Europe (Athanas et al., 2024).

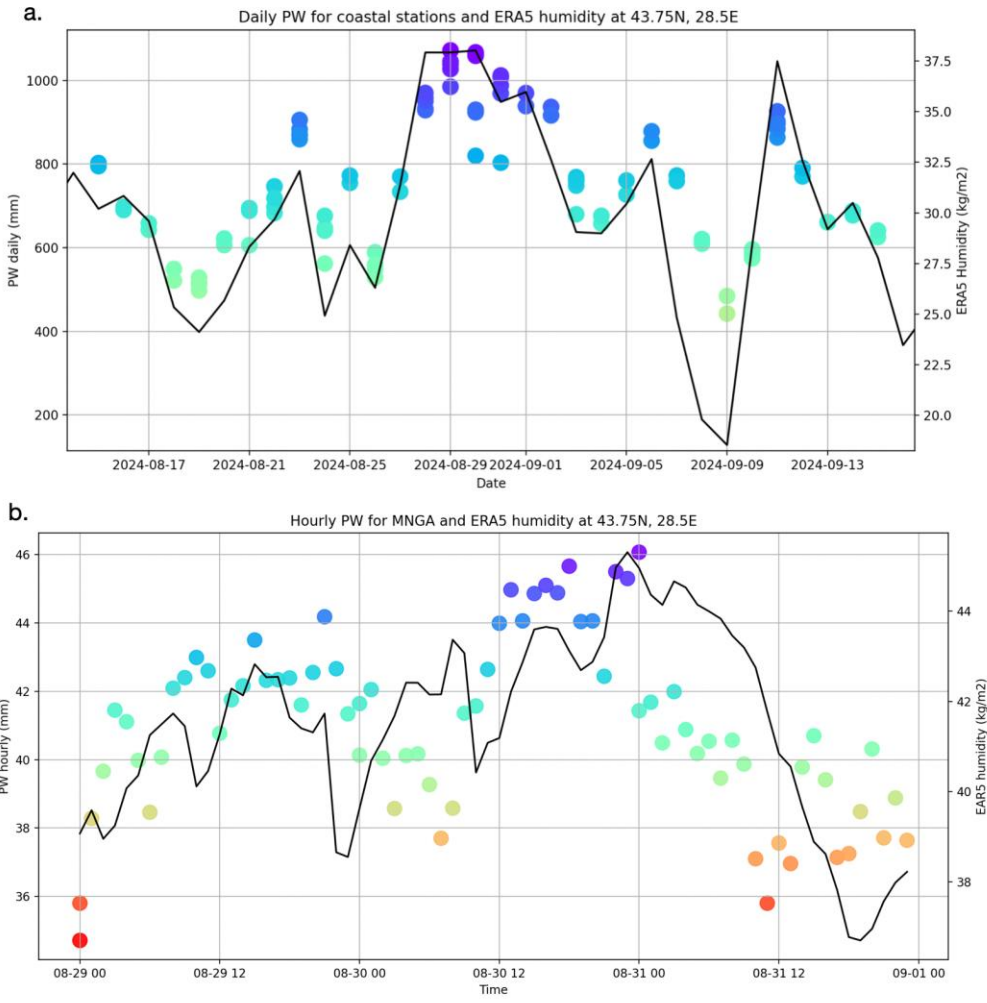
551 Elevated PWV was observed as early as ~~DOY 239~~ August 27th (Figure 12a), suggesting that the  
552 tropospheric moisture loading began to increase several days before the onset of the rainfall. This  
553 accelerated increase in PWV can serve as an early indicator of a developing weather system.  
554 Remarkably, although HAR1, located inland, did not directly experience the extreme rainfall, it  
555 exhibited similar PWV behavior to coastal stations, suggesting that GNSS stations, even outside  
556 the immediate storm zones, can capture atmospheric signals indicative of intense precipitation.  
557 This finding offers a valuable precedent, showing that PWV measurements at GNSS stations not  
558 directly in the storm's path can still provide critical insights into moisture dynamics at the  
559 tropospheric level. The comparison with ERA5's total-column water vapour further supports this  
560 interpretation, as the broad temporal evolution of ERA5 humidity mirrors the GNSS-derived daily  
561 PWV patterns, despite the inherently coarser resolution of the reanalysis data.



562

563 *Figure 11. a: Map of GNSS stations coloured as a function of PWV estimated for the 29th of August a day*  
564 *before the heavy rainfall in August 2024. b: Daily PWV values for each station, plotted as a function of*  
565 *their longitudinal distance relative to the city of Constanta. showing the difference between rainy days (red*  
566 *circles) and non-rainy days (coloured as a function of Julian day index).*

567 Shifting focus to Using the hourly PWV data, Figure 12b shows the results from illustrates the  
 568 evolution of water vapour at the MNGA station, which recorded the heaviest rainfall in the study  
 569 area. Notably, MNGA also showed a rapid buildup of PWV, reaching values greater than 44 mm/hr  
 570 just a few hours before the storm event. This rapid increase in PWV strongly suggests that the  
 571 accumulation of atmospheric moisture is a precursor to extreme weather events, such as intense  
 572 rainfall and storms. This observation aligns with known atmospheric dynamics, where a significant  
 573 increase in water vapor content precedes heavy precipitation, providing further evidence of the  
 574 potential for GNSS-based PWV monitoring to serve as an early warning tool for extreme weather.  
 575 The general rising trend toward the event is present in both GNSS-based and ERA5 reanalysis  
 576 datasets, although some minor fluctuations are not matched. After the storm the GNSS PWV drops  
 577 sharply while ERA5 maintains elevated values for several hours. These differences show that  
 578 GNSS can resolve rapid, real-time atmospheric changes that may be blurred in large-scale weather  
 579 model products.



580  
 581 *Figure 12. Comparison of GNSS-derived precipitable water vapor (coloured circles) with independent*  
 582 *humidity data (black line) from ERA5's total column vertically-integrated water vapor parameter. a. Daily*  
 583 *PWV values at selected GNSS stations (CONB, HARI, MNGA, MNGL, MNGM, TUZL) alongside daily-*  
 584 *averaged ERA5 humidity. b. Hourly PWV values at the MNGA GNSS station compared with hourly ERA5*

585 *humidity at the 43.75°N, 28.5°E grid point. on Time series of precipitable water vapour per day estimated*  
586 *at several GNSS stations (Figure 2), shown over the period of a month centered on the storm event*  
587 *(highlighted in blue); b. Hourly rates of PWV for station MNGA with the heaviest recorded rainfall at the*  
588 *location of the station, highlighted in blue.*

## 589 **5. Discussion**

590 Storm evolution, in the meteorological sense, describes the sequence of processes from pre-storm  
591 atmospheric moisture accumulation to convective initiation, peak rainfall, electrical activity, and  
592 the associated marine response along coastal areas. The multi-sensor dataset used here captures  
593 these different stages: GNSS-PWV documents the build-up of column water vapor before  
594 convective onset, infrasound detects lightning-generated acoustic waves and pressure disturbances  
595 during the mature convective phase, high-frequency seismic noise reflects the timing and spatial  
596 progression of intense rainfall at the surface, microseisms respond to storm-driven changes in sea  
597 state, and ERA5/MTG provide the mesoscale structure that ties these geophysical signals together.  
598 By observing the same storm through these complementary physical pathways, we can outline a  
599 more detailed picture of how the storm developed, intensified, and decayed than is possible from  
600 individual datasets.

601 The integration of infrasound, seismic, and GNSS data in monitoring the extreme storm event over  
602 the Black Sea provides valuable insights into the dynamics of storm behavior and demonstrates  
603 the potential of **repurposing** non-conventional sensors for meteorological analysis. Infrasound  
604 data, for instance, revealed a clear acoustic signature of lightning activity, with signals detected in  
605 the range of 0.6 to 7 Hz corresponding to electrical discharges. The high frequency of infrasound  
606 detections (around 1,100) supports its utility as a reliable tool for tracking storm-related  
607 phenomena, particularly lightning, which is difficult to capture with traditional methods. However,  
608 the signals did not always perfectly align with lightning strikes, indicating that other factors, such  
609 as the movement of storm systems or variations in atmospheric conditions, may influence  
610 infrasound signatures. This suggests that refining the correlation between infrasound signals and  
611 lightning activity could be an avenue for future research, particularly in cases of sparse lightning  
612 or in remote regions.

613 Seismic data alone also showed a strong connection between high-frequency seismic noise and  
614 heavy rainfall, supporting previous studies that linked seismic signals to rainfall intensity. The  
615 distinction between high-frequency and low-frequency seismic noise is particularly noteworthy.  
616 **Increases in high-frequency seismic noise occurred during** ~~correlated with~~ intense precipitation,  
617 while low-frequency signals were associated with wave height and storm-driven winds. This  
618 suggests that different seismic frequencies capture distinct storm dynamics, with high-frequency  
619 signals reflecting localized rainfall impacts and low-frequency signals tied to broader atmospheric  
620 and oceanic interactions. This dual-frequency approach provides a more nuanced interpretation of  
621 seismic data in storm monitoring, highlighting its complexity.

622 A key finding of this study is that K-means clustering of multiple acoustic features, including  
623 spectral centroids, roll-off, flux, and zero-crossing rate, effectively segmented the infrasound  
624 record into distinct storm phases. This approach proved more robust than relying on any single  
625 feature, as the combination captured the complex, evolving nature of the storm's acoustic signature.  
626 For instance, the identified clusters delineated periods of intense precipitation, elevated

627 background acoustic levels, and calm intervals, providing a data-driven overview of the storm's  
628 progression. The fact that these acoustically defined phases align with independent meteorological  
629 observations, such as rainfall peaks, confirms that the infrasound signal variability is a direct  
630 response to the storm's atmospheric dynamics.

631 Furthermore, the observed spectral similarity between the infrasound signals and high-frequency  
632 seismic envelopes suggests a coupled seismo-acoustic response to the storm. This implies that the  
633 same atmospheric forcing, such as pressure fluctuations from rainfall and wind, generates  
634 complementary signals in the atmosphere (infrasound) and the ground (seismic waves). Our  
635 findings are consistent with other studies of intense weather systems, where coupled microbarom-  
636 microseism signals have been shown to track storm structure and evolution (e.g., Butler & Aucan,  
637 2018; Smirnov, 2021). The coherent acoustic and seismic responses to atmospheric-oceanic  
638 pressures, as also documented in Distributed Acoustic Sensing studies (Taweessintananon et al.,  
639 2023) and surf studies (Francoeur et al., 2025), reinforce the interpretation of a shared source  
640 mechanism. Therefore, a major and logical next step is to move beyond analyzing these datasets  
641 in parallel and to perform joint clustering of seismo-acoustic data (e.g. Floroiu et al., 2025). Such  
642 an integrated approach could unlock a more comprehensive, multi-physics understanding of storm  
643 dynamics by simultaneously characterizing the coupled atmospheric and ground-borne wavefields.

644 ~~A key aspect of the analysis was the use of unsupervised learning methods, such as K-means~~  
645 ~~clustering, to identify patterns in the infrasound data. This approach segmented the infrasound~~  
646 ~~signals into distinct clusters, suggesting the evolution of different phases of the storm. By~~  
647 ~~identifying these phases, we can correlate shifts in spectral content with variations in storm~~  
648 ~~intensity. However, a major goal for future work is to perform joint clustering with seismic data,~~  
649 ~~which could provide a more comprehensive understanding of the storm's acoustic and seismic~~  
650 ~~dynamics. Seismic data, particularly high frequency seismic noise, closely resembled infrasound~~  
651 ~~spectral decay, suggesting a coupling between the two types of signals. This spectral similarity~~  
652 ~~may indicate that both infrasound and seismic signals are influenced by the same atmospheric and~~  
653 ~~oceanic processes, such as pressure fluctuations caused by rainfall, wind, and storm induced~~  
654 ~~waves. The coupling between seismic and infrasound signals further emphasizes the need to~~  
655 ~~integrate these data sources, as they capture different but complementary aspects of storm~~  
656 ~~behavior. Future studies using joint clustering techniques will be crucial in enhancing the detection~~  
657 ~~of storm phases and improving the understanding of the coupling between seismic and infrasound~~  
658 ~~data.~~

659 The temporal variations observed in GNSS-derived integrated precipitable water vapor provide  
660 valuable insights into atmospheric moisture dynamics before extreme weather events. The  
661 pronounced increase in PWV, particularly in the days leading up to and during the storm, supports  
662 the link between elevated atmospheric water vapor and precipitation. Notably, the buildup of PWV  
663 starting roughly three days before the extreme rainfall as early as DOY 239 suggests that rising  
664 moisture levels in the troposphere can serve as an early indicator of impending intense  
665 precipitation extreme rainfall. Even stations located up to 130 km inland, such as HAR1, recorded  
666 similar PWV trends, indicating that GNSS stations outside direct storm zones can still provide  
667 crucial atmospheric data. Hourly PWV trends further revealed a rapid increase several hours before  
668 precipitation, with values exceeding 44 mm/hr, highlighting the accumulation of moisture just  
669 before heavy rainfall. These findings align with the notion that increasing atmospheric moisture  
670 acts as a precursor to intense precipitation, highlighting the potential of GNSS-based PWV

671 monitoring as a real-time tool for tracking moisture and understanding short-term atmospheric  
672 fluctuations.

673 The integration of GNSS, infrasound, and seismic data provides a more comprehensive  
674 understanding of storm dynamics than any single data source alone. The synergy between these  
675 diverse sensor types allows for the detection of atmospheric moisture, lightning activity, rainfall-  
676 induced seismic signals, and storm-driven oceanic interactions. Future research should focus on  
677 refining unsupervised learning algorithms for infrasound and seismic signal classification,  
678 optimizing joint clustering techniques, and improving the integration of these data sources to  
679 enhance storm forecasting and early-warning systems. We believe this multi-sensor approach  
680 holds promise for improving our ability to predict extreme weather events, understand their  
681 impacts, and mitigate associated risks.

## 682 **6. Conclusions**

683 This study presents a comprehensive analysis of a record-breaking storm over the Black Sea, using  
684 a combination of GNSS, infrasound, and seismic data to capture the dynamics of extreme weather  
685 events. Our findings underscore the power of multi-sensor networks in enhancing the  
686 understanding of storm behavior, particularly in the context of atmospheric moisture, lightning  
687 activity, and storm-induced seismic signals. GNSS-derived integrated precipitable water vapor  
688 indicates a clear buildup of atmospheric moisture hours before the onset of heavy rainfall,  
689 providing valuable insights into the lead-up to extreme precipitation events. Infrasound and  
690 seismic data further complemented this analysis, with infrasound serving as a reliable tool for  
691 tracking lightning activity and seismic data revealing the link between rainfall intensity and high-  
692 frequency seismic noise.

693 The storm we analyzed is not only a significant meteorological event but also serves as a powerful  
694 example of how climate change may be influencing the frequency and intensity of extreme weather  
695 phenomena. Record-breaking storms like this are increasingly being recognized as evidence of  
696 shifting atmospheric conditions, driven by global climate change. The integration of GNSS,  
697 infrasound, and seismic data provides a more nuanced and holistic view of storm dynamics,  
698 highlighting the need for advanced monitoring systems to predict and respond to such extreme  
699 events. Moving forward, the combination of these innovative tools holds great potential for  
700 improving early-warning systems, enhancing storm forecasting, and better understanding the  
701 impacts of climate change on atmospheric and oceanic processes.

## 702 **7. Code availability**

703 Seismic data were processed with the open-source python framework for seismology Obspy  
704 (Beyreuther et al., 2010). Infrasound data was processed with the WinPMCC software (Le Pichon  
705 et al., 2010) developed by CEA/DASE (French Atomic Energy Commission, Environmental  
706 Assessment and Monitoring Department) and open-source Python libraries for signal processing.  
707 Some of the figures were made with GMT (Generic Mapping Tools, Wessel et al., 2019). The  
708 GNSS data was processed using Gamit/Globk (Herring et al., 2020) developed by Massachusetts  
709 Institute of Technology (<http://www-gpsg.mit.edu/gg/>).

## 710 **8. Data availability**

711 Seismic data are part of the Romanian National Seismic Network maintained by the National  
712 institute for Earth Physics (NIEP, [www.infp.ro](http://www.infp.ro)) and are freely available in the miniseed format via  
713 EIDA (European Integrated Data Archive, <https://www.orfeus-eu.org/data/eida/>). GNSS data are  
714 available for download from NIEP (<http://gps.infp.ro/#/download>) and are provided in the  
715 standardized RINEX v2 format, with 24-hour files sampled at 30-second intervals. Infrasound data  
716 at AGIR are available to download from NIEP via FDSN dataselect web service. Hourly hydro-  
717 meteorological data were obtained from the Copernicus Climate Change Service, Climate Data  
718 Store (<https://doi.org/10.24381/cds.bd0915c6>), ERA5 dataset (Hersbach et al., 2023). **Limited**  
719 **wind and precipitation data were downloaded from the National Meteorological Agency from**  
720 **<https://www.meteoromania.ro/grafice/>** (accessed on 13.09.2024) and from  
721 **[https://www.meteoromania.ro/clim/caracterizare-lunara/cc\\_2024\\_08.html](https://www.meteoromania.ro/clim/caracterizare-lunara/cc_2024_08.html)** (accessed on  
722 **10.11.2025**), respectively. Lightning data came from Meteosat Third Generation Lightning Imager  
723 operated by EUMETSAT (The European Organisation for the Exploitation of Meteorological  
724 Satellites, <https://www.eumetsat.int/>).

## 725 **9. Author contribution**

726 **Laura Petrescu:** Conceptualization, Methodology, Software, Formal analysis, Data Curation,  
727 Writing-Original Draft, Visualization, Funding acquisition; **Bogdan Antonescu:**  
728 Conceptualization, Writing-Review & Editing, Visualization; **Sorin Nistor:** Software, Formal  
729 Analysis, Data curation, Visualisation, Writing-Review & Editing; **Iustin Floroiu:** Methodology,  
730 Software, Formal analysis, Data Curation, Writing-Original Draft, Visualization; **Dragoş Ene:**  
731 Software, Formal analysis, Data Curation, Writing-Review & Editing; **Daniela Ghica:** Software,  
732 Formal analysis, Data Curation; **Constantin Ionescu:** Funding Acquisition, Resources, Project  
733 administration; **Andrei Anghel:** Methodology, Supervision; **Mihai Datcu:** Methodology,  
734 Supervision, Funding Acquisition, Resources, Project administration.

## 735 **10. Acknowledgments**

736 We would like to thank the technicians and staff at NIEP for their support in installing,  
737 maintaining, and ensuring the proper functioning of the equipment used in this study. Additionally,  
738 we appreciate the efforts of those involved in data formatting and preparation (Cristian Neagoe,  
739 Eduard Nastase, Victorin Toader) which were essential for this work. **We also thank the two**  
740 **anonymous reviewers for their valuable feedback, which helped improve the manuscript.**

## 741 **11. Financial support:**

742 This work was carried out in the framework of the “Competence Center for Climate Change Digital  
743 Twin for Earth forecasts and societal redressment” Project PNRR- DTEClimate nr.  
744 760008/31.12.2023, subproject Reactive “The Research center for climate change due to natural  
745 disasters and extreme weather events”, supported by the Ministry of Research, Innovation and  
746 Digitalization of Romania.

747

## 748 **12. References**

749 Antonescu, B., Dafis, S., & Faranda, D.: Changes in precipitation patterns driving August 2024  
750 Romania floods mostly driven by human-driven climate change. *ClimaMeter, Institut Pierre*  
751 *Simon Laplace, CNRS*. <https://doi.org/10.5281/zenodo.14056214>, 2018.

752 Ardhuin, F., Gualtieri, L., Stutzmann, E., Nakata, N. and Fichtner, A.: Physics of ambient noise  
753 generation by ocean waves. In *Seismic ambient noise*, Eds: Nakata, N., Gualtieri, L., Fichtner, A.  
754 Cambridge University Press, 69-108, <https://doi.org/10.1017/9781108264808.005>, 2019.

755 [Assink, J. D., Evers, L. G., Holleman, I., and Paulssen, H.: Characterization of infrasound from](#)  
756 [lightning, \*Geophysical Research Letters\*, 35, L15802, <https://doi.org/10.1029/2008GL034193>,](#)  
757 [2008.](#)

758 Aster, R.C., McNamara, D.E. & Bromirski, P.D.: Multidecadal climate-induced variability in  
759 microseisms. *Seismological Research Letters*, 79(2), 194-202,  
760 <https://doi.org/10.1785/gssrl.79.2.194>, 2008.

761 Aster, R.C., Ringler, A.T., Anthony, R.E., & Lee, T.A.: Increasing ocean wave energy observed  
762 in Earth's seismic wavefield since the late 20th century. *Nature Communications*, 14(1), 6984,  
763 <https://doi.org/10.1038/s41467-023-42673-w>, 2023.

764 Athanase, M., Sánchez-Benítez, A., Monfort, E., Jung, T. and Goessling, H.F.: How climate  
765 change intensified storm Boris' extreme rainfall, revealed by near-real-time storylines.  
766 *Communications Earth & Environment*, 5(1), 676, <https://doi.org/10.1038/s43247-024-01847-0>,  
767 2024.

768 Awange, J.L.: Environmental monitoring using GNSS: Global navigation satellite systems,  
769 Springer, Heidelberg, <https://doi.org/10.1007/978-3-540-88256-5>, 2012.

770 Beyreuther, M., Barsch, R., Krischer, L., Megies, T., Behr, Y. and Wassermann, J.: ObsPy: A  
771 Python toolbox for seismology. *Seismological Research Letters*, 81(3), 530-533,  
772 <https://doi.org/10.1785/gssrl.81.3.530>, 2010.

773 Bengtsson, L., Hodges, K.I. and Roeckner, E.: Storm tracks and climate change. *Journal of*  
774 *climate*, 19(15), 3518-3543, <https://doi.org/10.1175/JCLI3815.1>, 2006.

775 Bollinger, L., Perrier, F., Avouac, J.P., Sapkota, S., Gautam, U., Tiwari, D.R.: Seasonal  
776 modulation of seismicity in the Himalaya of Nepal, *Geophysical Research Letters*, 34(8),  
777 <https://doi.org/10.1029/2006GL029192>, 2007.

778 Bondár, I., Šindelářová, T., Ghica, D., Mitterbauer, U., Liashchuk, A., Baše, J., Chum, J., Czanik,  
779 C., Ionescu, C., Neagoe, C. and Pásztor, M.: Central and Eastern European Infrasound Network:  
780 contribution to infrasound monitoring, *Geophysical Journal International*, 230(1), 565-579,  
781 <https://doi.org/10.1093/gji/ggac066>, 2022.

782 Borzi, A.M., Minio, V., Cannavò, F., Cavallaro, A., D'Amico, S., Gauci, A., De Plaen, R., Lecocq,  
783 T., Nardone, G., Orasi, A., Picone, M., Cannata, A.: Monitoring extreme meteo-marine events in  
784 the Mediterranean area using the microseism (Medicane Apollo case study). *Scientific Reports*,  
785 12(1), <https://doi.org/10.1038/s41598-022-25395-9>, 2022.

786 Bosy, J., Kaplon, J., Rohm, W., Sierny, J. and Hadas, T.: Near real-time estimation of water vapour  
787 in the troposphere using ground GNSS and the meteorological data, *Annales Geophysicae*, 30,  
788 1379–1391, <https://doi.org/10.5194/angeo-30-1379-2012>, 2012.

789 Brachet, N., Brown, D., Le Bras, R., Cansi, Y., Mialle, P., Coyne, J.: Monitoring the Earth's  
790 Atmosphere with the Global IMS Infrasound Network, in: *Infrasound Monitoring for Atmospheric*  
791 *Studies*, edited by: Le Pichon, A., Blanc, E., Hauchecorne, A. , Springer, Dordrecht,  
792 [https://doi.org/10.1007/978-1-4020-9508-5\\_3](https://doi.org/10.1007/978-1-4020-9508-5_3), 2010.

793 Bromirski, P.D. and Duennebier, F.K.: The near-coastal microseism spectrum: Spatial and  
794 temporal wave climate relationships. *Journal of Geophysical Research: Solid Earth*, 107(B8), ESE  
795 5-1-ESE 5-20, <https://doi.org/10.1029/2001JB000265>, 2002.

796 Bruyninx, C., Habrich, H., Söhne, W., Kenyeres, A., Stangl, G. and Völksen, C.: Enhancement of  
797 the EUREF permanent network services and products, in: *Proceedings of the International*  
798 *Association of Geodesy, Symposium on Geodesy for Planet Earth, Buenos Aires, Argentina, 31*  
799 *August-4 September 2009, 27-34*, 2012.

800 Burtin, A., Hovius, N. and Turowski, J.M.: Seismic monitoring of torrential and fluvial processes.  
801 *Earth Surface Dynamics*, 4(2), 285-307, <https://doi.org/10.5194/esurf-4-285-2016>, 2016.

802 [Butler, R. and Aucan, J.: Multisensor, microseismic observations of a hurricane transit near the](#)  
803 [ALOHA cabled observatory. \*Journal of Geophysical Research: Solid Earth\*, 123\(4\), 3027-3046,](#)  
804 [2018.](#)

805 Campus, P. and Christie, D.R.: Worldwide observations of infrasonic waves, in: *Infrasound*  
806 *monitoring for atmospheric studies*, edited by: Le Pichon, A., Blanc, E., Hauchecorne, A.,  
807 Springer, Dordrecht, Netherlands, 185-234, [https://doi.org/10.1007/978-1-4020-9508-5\\_6](https://doi.org/10.1007/978-1-4020-9508-5_6), 2009.

808 Cansi, Y. and Pichon, A.L.: Infrasound event detection using the progressive multi-channel  
809 correlation algorithm, in: *Handbook of signal processing in acoustics.*, edited by: Havelock, D.,  
810 Kuwano, S., Vorländer, M., Springer, New York, 1425-1435, [https://doi.org/10.1007/978-0-387-](https://doi.org/10.1007/978-0-387-30441-0_77)  
811 [30441-0\\_77](#), 2008.

812 [Coates, A. and Ng, A.Y.: Learning feature representations with k-means. In \*Neural Networks:\*](#)  
813 [Tricks of the Trade: Second Edition \(561-580\). Berlin, Heidelberg: Springer Berlin Heidelberg,](#)  
814 [2012.](#)

815 Coviello, V., Palo, M., Adirosi, E. and Picozzi, M.: Seismic signature of an extreme hydro-  
816 meteorological event in Italy, *Natural Hazards*, 1(1), 17, [https://doi.org/10.1038/s44304-024-](https://doi.org/10.1038/s44304-024-00018-7)  
817 00018-7, 2024.

818 Diaz, J., Ruiz, M., Udina, M., Polls, F., Martí, D., Bech, J.: Monitoring storm evolution using a  
819 high-density seismic network, *Scientific Reports*, 13(1), [https://doi.org/10.1038/s41598-023-](https://doi.org/10.1038/s41598-023-28902-8)  
820 28902-8, 2023.

821 [Díaz, J., Ruiz, M., Sánchez-Pastor, P.S. and Romero, P.: Urban seismology: On the origin of earth](#)  
822 [vibrations within a city. \*Scientific reports\*, 7\(1\), 15296, 2017.](#)

823 Dimitriu, R.G., Stanciu, I.M., Barbu M.-B., Dobrev, N., Dumitru, P.: First results on the western  
824 Black Sea coast geodynamics resulted from GeoPontica permanent GNSS stations network data  
825 processing, in: Proceedings of the 17th International Multidisciplinary Scientific GeoConference  
826 SGEM, Albena, Bulgaria August 2017, 17(11), 149-157, 2017.

827 [Dullaart, J.C., Muis, S., Bloemendaal, N. and Aerts, J.C.: Advancing global storm surge modelling](#)  
828 [using the new ERA5 climate reanalysis. \*Climate Dynamics\*, 54\(1\), 1007-1021, 2020.](#)

829 Ebeling, C.W.: Inferring Ocean Storm Characteristics from Ambient Seismic Noise. A Historical  
830 Perspective, *Advances in Geophysics*, 53, 1-33. [https://doi.org/10.1016/B978-0-12-380938-](https://doi.org/10.1016/B978-0-12-380938-4.00001-X)  
831 4.00001-X, 2012.

832 Faranda, D., Messori, G., Coppola, E., Alberti, T., Vrac, M., Pons, F., Yiou, P., Saint Lu, M., Hisi,  
833 A. N. S., Brockmann, P., Dafis, S., Mengaldo, G., and Vautard, R.: ClimaMeter: contextualizing  
834 extreme weather in a changing climate, *Weather Climate Dynamics*, 5, 959–983,  
835 <https://doi.org/10.5194/wcd-5-959-2024>, 2024.

836 [Floroiu, I., Anghel, A., Petrescu, L. and Datcu, M.: Clustering and Feature-Based Similarity](#)  
837 [Retrieval of Infrasound Events during Two Storms in Constanța, Romania, \*International\*](#)  
838 [Conference on Machine Intelligence for GeoAnalytics and Remote Sensing \(MIGARS\), Bucharest,](#)  
839 [Romania, 2025, 1–4, <https://doi.org/10.1109/MIGARS67156.2025.11231952>, 2025.](#)

840 [Francoeur, J.W., Matoza, R.S., Ortiz, H.D. and De Negri, R.: Identification of transient seismo-](#)  
841 [acoustic signals from crashing ocean waves: template matching and location of discrete surf](#)  
842 [events. \*Geophysical Journal International\*, 243\(2\), ggaf317, 2025.](#)

843 [Garcés, M.A.: On infrasound standards, part 1 time, frequency, and energy scaling. \*InfraMatics\*,](#)  
844 [2\(2\),13–35, <https://doi.org/10.4236/inframatics.2013.22002>, 2013.](#)

845 [Gastmeier, W.J. and Howe, B.: Recent studies of infrasound from industrial sources. \*Canadian\*](#)  
846 [Acoustics](#), 36(3), 58-59, 2008.

847 [Grafkina, M.V., Nyunin, B.N. and Sviridova, E.Y: Environmental monitoring and simulation of](#)  
848 [infrasound generating mechanism of traffic flow. \*Journal of Ecological Engineering\*, 20\(7\),](#)  
849 [2019.](#)

850 Grevemeyer, I., Herber, R. and Essen, H.H.: Microseismological evidence for a changing wave  
851 climate in the northeast Atlantic Ocean. *Nature*, 408(6810), 349-352,  
852 <https://doi.org/10.1038/35042558>, 2000.

853 Groos, J.C. and Ritter, J.R.R.: Time domain classification and quantification of seismic noise in  
854 an urban environment. *Geophysical Journal International*, 179(2), pp.1213-1231, 2009.

855 Gualtieri, L., Camargo, S.J., Pascale, S., Pons, F.M.E., & Ekström, G.: The persistent signature of  
856 tropical cyclones in ambient seismic noise, *Earth and Planetary Science Letters*, 484, 287-294.  
857 <https://doi.org/10.1016/j.epsl.2017.12.026>, 2018.

858 Guerova, G., Jones, J., Douša, J., Dick, G., de Haan, S., Pottiaux, E., Bock, O., Pacione, R.,  
859 Elgered, G., Vedel, H. and Bender, M.: Review of the state of the art and future prospects of the  
860 ground-based GNSS meteorology in Europe, *Atmospheric Measurement Techniques*, 9(11),  
861 5385–5406, <https://doi.org/10.5194/amt-9-5385-2016>, 2016.

862 Herring, T., King, R., Floyd, M., McClusky, S.: GAMIT Reference Manual GPS Analysis at MIT  
863 Release 10.7. GAMIT/GLOBK, 2020.

864 Hersbach, H., Bell, B., Berrisford, P., Hirahara, S., Horányi, A., Muñoz-Sabater, J., Nicolas, J.,  
865 Peubey, C., Radu, R., Schepers, D. and Simmons, A.: The ERA5 global reanalysis, *Quarterly*  
866 *Journal of the Royal Meteorological Society*, 146(730), 1999-2049, 2020.

867 Hersbach, H., Bell, B., Berrisford, P., Biavati, G., Horányi, A., Muñoz Sabater, J., Nicolas, J.,  
868 Peubey, C., Radu, R., Rozum, I., Schepers, D., Simmons, A., Soci, C., Dee, D., Thépaut, J.-N.:  
869 ERA5 hourly data on single levels from 1940 to present. Copernicus Climate Change Service  
870 (C3S) Climate Data Store (CDS), <https://doi.org/10.24381/cds.adbb2d47>, 2023.

871 Holmlund, K., Grandell, J., Schmetz, J., Stuhlmann, R., Bojkov, B., Munro, R., Lekouara, M.,  
872 Coppens, D., Viticchie, B., August, T. and Theodore, B.: Meteosat Third Generation (MTG):  
873 Continuation and innovation of observations from geostationary orbit, *Bulletin of the American*  
874 *Meteorological Society*, 102(5), E990-E1015, <https://doi.org/10.1175/BAMS-D-19-0304.1>, 2021.

875 Hua, J., Wu, M., Mulholland, J.P., Neelin, J.D., Tsai, V.C. and Trugman, D.T.: High-resolution  
876 precipitation monitoring with a dense seismic nodal array. *Scientific Reports*, 13(1), 11450,  
877 <https://doi.org/10.1038/s41598-023-38008-w>, 2023.

878 Hupe, P., Ceranna, L., Pilger, C., de Carlo, M., Le Pichon, A., Kaifler, B. and Rapp, M.: Assessing  
879 middle atmosphere weather models using infrasound detections from microbaroms. *Geophysical*  
880 *Journal International*, 216(3), 1761-1767, <https://doi.org/10.1093/gji/ggy520>, 2019.

881 Hupe, P., Ceranna, L., Le Pichon, A., Matoza, R.S. and Mialle, P.: International Monitoring  
882 System infrasound data products for atmospheric studies and civilian applications. *Earth System*  
883 *Science Data Discussions*, 14, 4201–4230, <https://doi.org/10.5194/essd-14-4201-2022>, 2022.

- 884 Iliescu, A. I., Rus, T., Danciu, V., Moldoveanu, C., & Ilie, A.: Current situation of GNSS networks  
885 in Romania, *Bulletin of University of Agricultural Sciences and Veterinary Medicine Cluj-Napoca.*  
886 *Horticulture*, 76(2), 2019.
- 887 Jakobsen, J.: Infrasound emission from wind turbines. *Journal of low frequency noise, vibration*  
888 *and active control*, 24(3), 145-155, 2005.
- 889 Jiao, D., Xu, N., Yang, F. and Xu, K.: Evaluation of spatial-temporal variation performance of  
890 ERA5 precipitation data in China. *Scientific Reports*, 11(1), 17956, 2021.
- 891 Johnston, G., Riddell, A. and Hausler, G.: The international GNSS service, in: Springer handbook  
892 of global navigation satellite systems, edited by: Teunissen, P.J. and Montenbruck, O., Springer,  
893 Cham, Switzerland, 967-982, [https://doi.org/10.1007/978-3-319-42928-1\\_33](https://doi.org/10.1007/978-3-319-42928-1_33), 2017.
- 894 Jones, J., Guerova, G., Douša, J., Dick, G., de Haan, S., Pottiaux, E., Bock, O., Pacione, R. and  
895 Van Malderen, R.: Advanced GNSS tropospheric products for monitoring severe weather events  
896 and climate, COST Action ES1206 Final Action Dissemination Report, 563, 2020.
- 897 Karabatić, A., Weber, R. and Haiden, T.: Near real-time estimation of tropospheric water vapour  
898 content from ground based GNSS data and its potential contribution to weather now-casting in  
899 Austria, *Advances in Space Research*, 47(10), 1691–1703,  
900 <https://doi.org/10.1016/j.asr.2010.10.028>, 2011.
- 901 Kober, K. and Tafferner, A.: Tracking and nowcasting of convective cells using remote sensing  
902 data from radar and satellite, *Meteorologische Zeitschrift*, 1(18), 75-84,  
903 <https://doi.org/10.1127/0941-2948/2009/359>, 2009.
- 904 Koper, K.D. & Burlacu, R.: The fine structure of double-frequency microseisms recorded by  
905 seismometers in North America. *Journal of Geophysical Research: Solid Earth*, 120(3), 1677-  
906 1691. <https://doi.org/10.1002/2014JB011820>, 2015.
- 907 Landès, M., Ceranna, L., Le Pichon, A. and Matoza, R.S.: Localization of microbarom sources  
908 using the IMS infrasound network. *Journal of Geophysical Research: Atmospheres*, 117(D6),  
909 <https://doi.org/10.1029/2011JD016684>, 2012.
- 910 Landskron, D., Böhm, J.: VMF3/GPT3: refined discrete and empirical troposphere mapping  
911 functions, *Journal of Geodesy*, 92, 349–360, <https://doi.org/10.1007/s00190-017-1066-2>, 2018.
- 912 Li, L., Boué, P., Retailleau, L., & Campillo, M.: Spatiotemporal Correlation Analysis of Noise-  
913 Derived Seismic Body Waves With Ocean Wave Climate and Microseism Sources, *Geochemistry,*  
914 *Geophysics, Geosystems*, 21(9), <https://doi.org/10.1029/2020GC009112>, 2020.
- 915 Listowski, C., Forestier, E., Dafis, S., Farges, T., De Carlo, M., Grimaldi, F., Le Pichon, A.,  
916 Vergoz, J., Heinrich, P. and Claud, C.: Remote monitoring of Mediterranean hurricanes using  
917 infrasound, *Remote Sensing*, 14(23), 6162, <https://doi.org/10.3390/rs14236162>, 2022.

918 MacQueen, J.: Some methods for classification and analysis of multivariate observations, in:  
919 Proceedings of the Fifth Berkeley Symposium on Mathematical Statistics and Probability,  
920 Berkeley, California, January 1967, 5, 281-298, 1967.

921 Marut, G., Hadas, T., Kaplon, J., Trzcina, E. and Rohm, W.: Monitoring the water vapor content  
922 at high spatio-temporal resolution using a network of low-cost multi-GNSS receivers, *IEEE*  
923 *Transactions on Geoscience and Remote Sensing*, 60, 1-14,  
924 <https://doi.org/10.1109/TGRS.2022.3226631>, 2022.

925 Pásztor, M., Czanik, C. and Bondár, I.: A single array approach for infrasound signal  
926 discrimination from quarry blasts via machine learning, *Remote Sensing*, 15(6), 1657,  
927 <https://doi.org/10.3390/rs15061657>, 2023.

928 Le Pichon, A., Matoza, R., Brachet, N. and Cansi, Y.: Recent enhancements of the PMCC  
929 infrasound signal detector. *Inframatrics*, 26, 5-8, 2010.

930 [Price, I., Sanchez-Gonzalez, A., Alet, F., Andersson, T.R., El-Kadi, A., Masters, D., Ewalds, T.,](#)  
931 [Stott, J., Mohamed, S., Battaglia, P. and Lam, R.: Probabilistic weather forecasting with machine](#)  
932 [learning. \*Nature\*, 637\(8044\), 84-90, 2025](#)

933 Priego, E., Jones, J., Porres, M.J. and Seco, A.: Monitoring water vapour with GNSS during a  
934 heavy rainfall event in the Spanish Mediterranean area, *Geomatics, Natural Hazards and Risk*,  
935 8(2), 282–294, <https://doi.org/10.1080/19475705.2016.1201150>, 2017.

936 Retailleau, L. & Gualtieri, L.: Multi-phase seismic source imprint of tropical cyclones, *Nature*  
937 *Communications*, 12(1), <https://doi.org/10.1038/s41467-021-22231-y>, 2021.

938 Rindraharisaona, E.J., Réchou, A., Fontaine, F.R., Barruol, G., Stamenoff, P., Boudevillain, B.,  
939 Rigaud-Louise, F. and Delcher, E.: Seismic signature of rain and wind inferred from seismic data,  
940 *Earth and Space Science*, 9(10), p.e2022EA002328, 2022.

941 [Šindelářová, J., Chum, J., Skripnikova, K., and Base, J.: Atmospheric infrasound observed during](#)  
942 [intense convective storms on 9–10 July 2011, \*Journal of Atmospheric and Solar-Terrestrial\*](#)  
943 [Physics, 122, 66–74, <https://doi.org/10.1016/j.jastp.2014.10.014>, 2015.](#)

944 [Šindelářová, T., De Carlo, M., Czanik, C., Ghica, D., Kozubek, M., Podolská, K., Baše, J., Chum,](#)  
945 [J., and Mitterbauer, U.: Infrasound signature of the post-tropical storm Ophelia at the Central and](#)  
946 [Eastern European Infrasound Network, \*Journal of Atmospheric and Solar-Terrestrial Physics\*, 217,](#)  
947 [105603, <https://doi.org/10.1016/j.jastp.2021.105603>, 2021.](#)

948 Smirnov, A., De Carlo, M., Le Pichon, A., Shapiro, N.M. and Kulichkov, S.: Characterizing the  
949 oceanic ambient noise as recorded by the dense seismo-acoustic Kazakh network. *Solid Earth*,  
950 12(2), 503-520, 2021.

951 Soci, C., Hersbach, H., Simmons, A., Poli, P., Bell, B., Berrisford, P., Horányi, A., Muñoz-Sabater,  
952 J., Nicolas, J., Radu, R. and Schepers: The ERA5 global reanalysis from 1940 to 2022. *Quarterly*  
953 *Journal of the Royal Meteorological Society*, 150(764), 4014-4048, 2024.

954 Sokol, Z., Szturc, J., Orellana-Alvear, J., Popova, J., Jurczyk, A. and Céleri, R.: The role of  
955 weather radar in rainfall estimation and its application in meteorological and hydrological  
956 modelling—A review, *Remote Sensing*, 13(3), 351, 2021.

957 Stopa, J.E., Cheung, K.F., Garcés, M.A. and Badger, N.: Atmospheric infrasound from nonlinear  
958 wave interactions during Hurricanes Felicia and Neki of 2009, *Journal of Geophysical Research:*  
959 *Oceans*, 117(C12), <https://doi.org/10.1029/2012JC008257>, 2012

960 Stott, P.: How climate change affects extreme weather events. *Science*, 352(6293), 1517-1518,  
961 <https://doi.org/10.1126/science.aaf7271>, 2016.

962 Tanimoto, T. & Anderson, A.: Seismic noise between 0.003 Hz and 1.0 Hz and its classification,  
963 *Progress in Earth and Planetary Science*, 10(1), <https://doi.org/10.1186/s40645-023-00587-7>,  
964 2023.

965 Taweesintananon, K., Landrø, M., Potter, J.R., Johansen, S.E., Rørstadbotnen, R.A., Bouffaut, L.,  
966 Kriesell, H.J., Brenne, J.K., Haukanes, A., Schjelderup, O. and Storvik, F.: Distributed acoustic  
967 sensing of ocean-bottom seismo-acoustics and distant storms: A case study from Svalbard,  
968 Norway. *Geophysics*, 88(3), B135-B150, 2023.

969 Tiberia, A., Mascitelli, A., D’adderio, L.P., Federico, S., Marisaldi, M., Porcù, F., Realini, E.,  
970 Gatti, A., Ursi, A., Fuschino, F. and Tavani, M.: Time evolution of storms producing terrestrial  
971 gamma-ray flashes using ERA5 reanalysis data, GPS, lightning and geostationary satellite  
972 observations. *Remote Sensing*, 13(4), 784, 2021.

973 Vaquero-Martínez, J. and Antón, M.: Review on the role of GNSS meteorology in monitoring  
974 water vapor for atmospheric physics, *Remote Sensing*, 13(12), 2287,  
975 <https://doi.org/10.3390/rs13122287>, 2021.

976 Viticchie, B., Lekouara, M., Hungershofer, K., Joro, S., Grandell, J., Maufrais, A., Marquez, M.J.,  
977 Munro, R.: Algorithm Theoretical Basis Document (ATBD) for L2 processing of the MTG  
978 Lightning Imager data, Rapp. Tech. EUMESTAT, 6, 2020.

979 Waxler, R., Frazier, W. G., Talmadge, C. L., Liang, B., Hetzer, C., Buchanan, H., and Audette, W.  
980 E.: Analysis of infrasound array data from tornadic storms in the southeastern United States,  
981 *Journal of the Acoustical Society of America*, 156, 1903–1919,  
982 <https://doi.org/10.1121/10.0028815>, 2024.

983 Wessel, P., Luis, J.F., Uieda, L.A., Scharroo, R., Wobbe, F., Smith, W.H. and Tian, D.: The generic  
984 mapping tools version 6, *Geochemistry, Geophysics, Geosystems*, 20(11), 5556-5564,  
985 <https://doi.org/10.1029/2019GC008515>, 2019.

986 Wilgan, K., Rohm, W. and Bosy, J.: Multi-observation meteorological and GNSS data comparison  
987 with numerical weather prediction model, *Atmospheric Research*, 156, 29–42,  
988 <https://doi.org/10.1016/j.atmosres.2014.12.011>, 2015.

989 Wu, G., Qin, S., Mao, Y., Ma, Z. and Shi, C.: Validation of precipitation events in ERA5 to gauge  
990 observations during warm seasons over eastern China. *Journal of Hydrometeorology*, 23(5), 807-  
991 822, 2022.

992

993

994

995

996

997

998

999

1000

1001

1002

1003

1004

1005

1006

1007

1008

1009

1010

1011

1012

1013